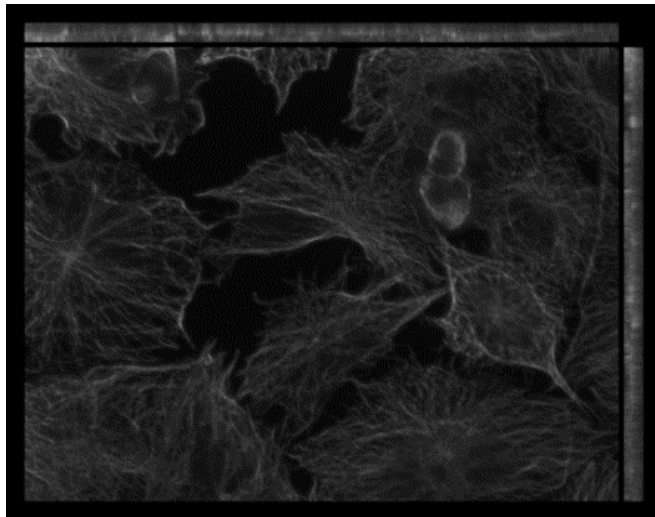


# DTE / MT bundling - overview

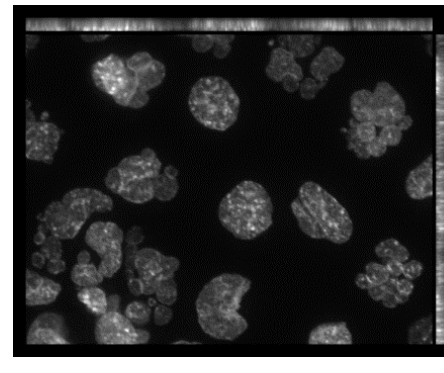
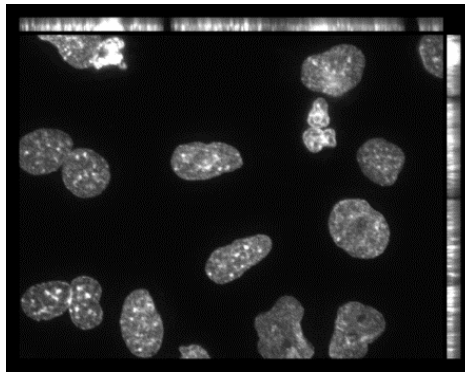
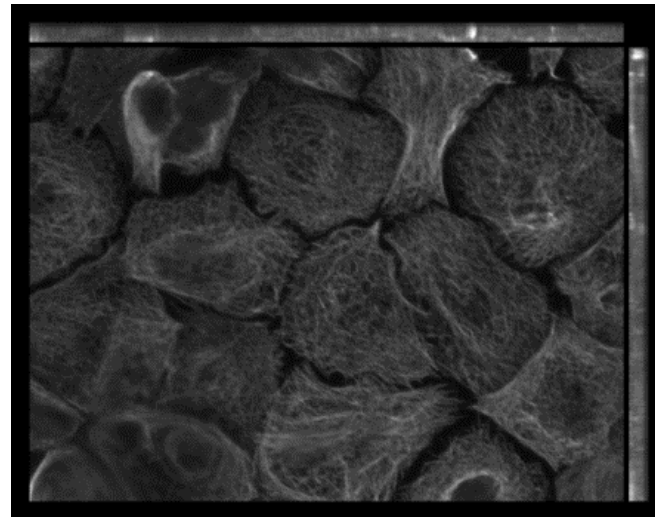
A. Matov March 2013

# DTE -> MT area -> find outline (AZ 521)

Untreated



Doc 10 nM



# Voronoi-Based Segmentation of Cells on Image Manifolds

Thouis R. Jones<sup>1</sup>, Anne Carpenter<sup>2</sup>, and Polina Golland<sup>1</sup>

<sup>1</sup> MIT CSAIL, Cambridge, MA, USA

<sup>2</sup> Whitehead Institute for Biomedical Research, Cambridge, MA, USA

**Abstract.** We present a method for finding the boundaries between adjacent regions in an image, where “seed” areas have already been identified in the individual regions to be segmented. This method was motivated by the problem of finding the borders of cells in microscopy images, given a labelling of the nuclei in the images. The method finds the Voronoi region of each seed on a manifold with a metric controlled by local image properties. We discuss similarities to other methods based on image-controlled metrics, such as Geodesic Active Contours, and give a fast algorithm for computing the Voronoi regions. We validate our method against hand-traced boundaries for cell images.

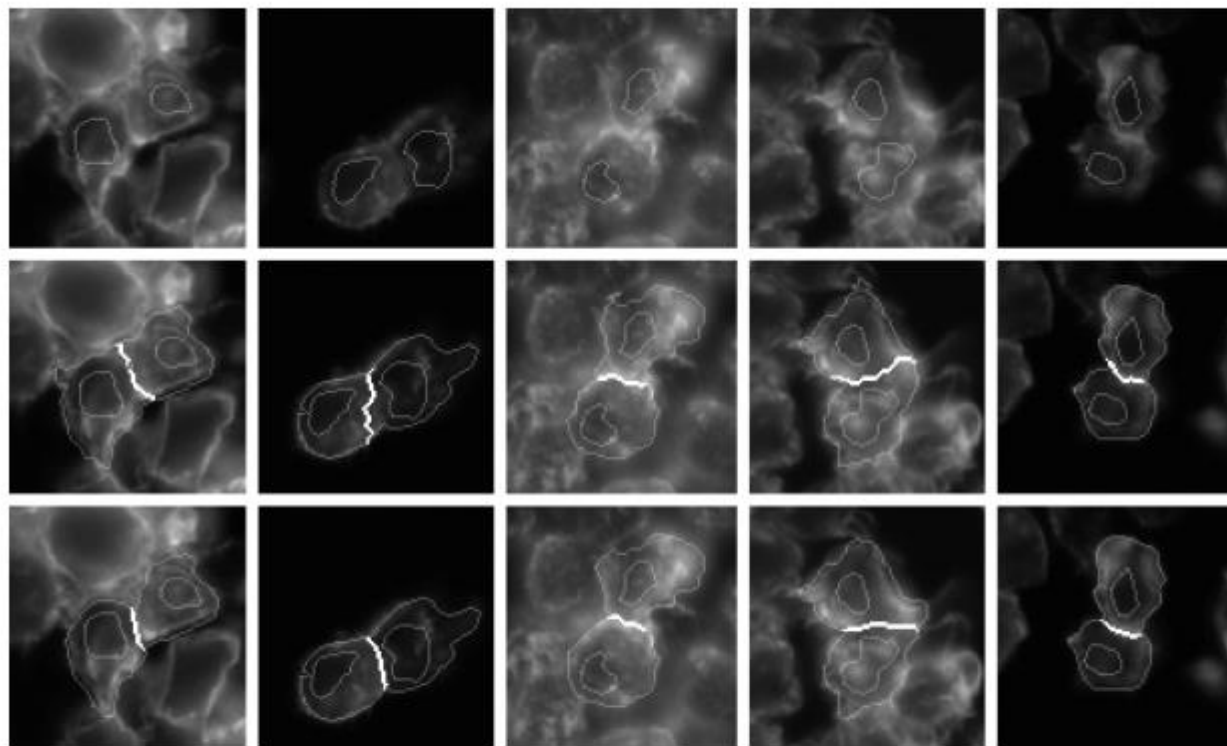
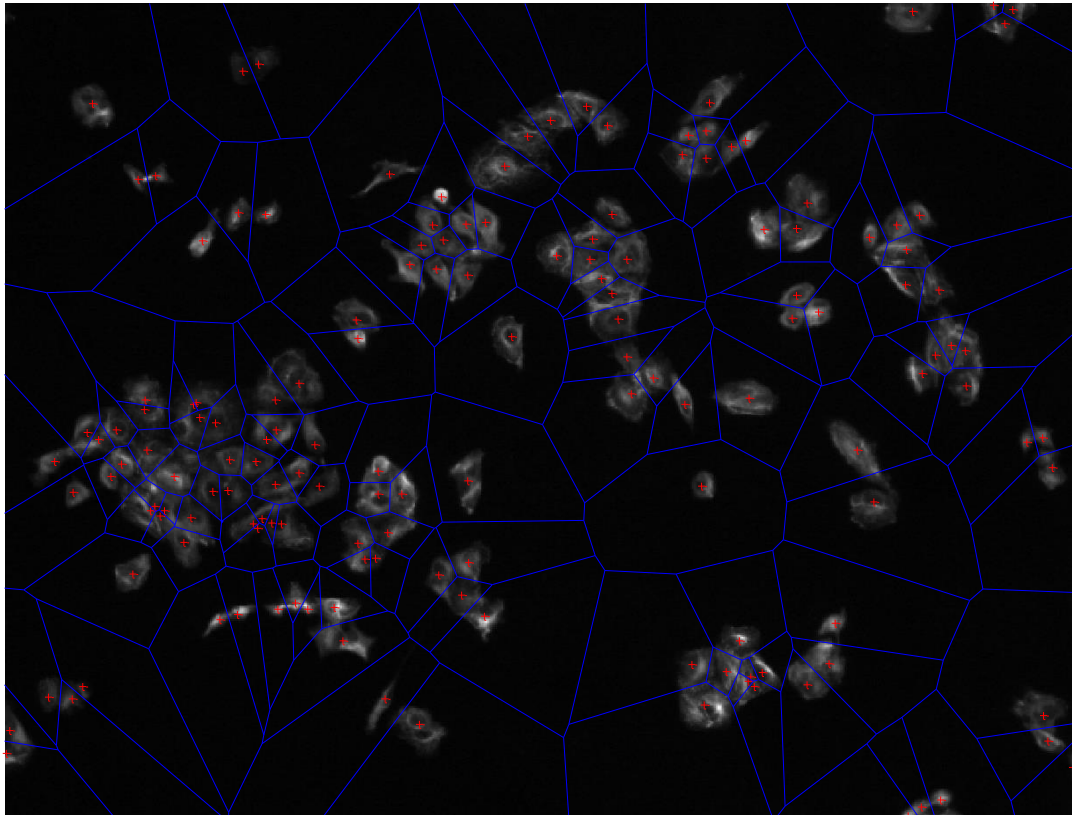


**Fig. 1.** Typical results from our algorithm. Internal shapes are seed regions, taken from manual segmentation of nuclei, and are the same in both rows. Bold lines show cell/cell boundaries that are compared. Top row: Cell images, with nuclei outlined. Middle row: Automatic segmentation with our method. Bottom row: Manual segmentation.

# Voronoi diagram- BRACA1 MTs in CTL cells



DAPI channel – unimodal  
thresholding to segment  
nuclei

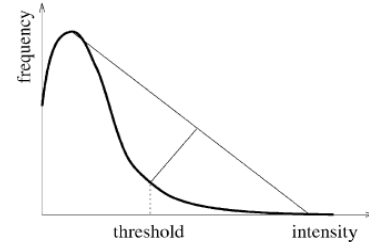


Fig. 1. Procedure for determining threshold from intensity histogram.

Then use the centroids (red)  
to build the Voronoi

# Task 2

- After treatment, analyze the morphology and intensity of the Tubulin channel

# Inferring Biological Structures from Super-Resolution Single Molecule Images Using Generative Models

Suvrajit Maji<sup>1</sup>, Marcel P. Bruchez<sup>1,2,3\*</sup>

**1** Lane Center for Computational Biology, School of Computer Science, Carnegie Mellon University, Pittsburgh, Pennsylvania, United States of America, **2** Department of Biological Sciences, Carnegie Mellon University, Pittsburgh, Pennsylvania, United States of America, **3** Department of Chemistry, Carnegie Mellon University, Pittsburgh, Pennsylvania, United States of America

## Abstract

Localization-based super resolution imaging is presently limited by sampling requirements for dynamic measurements of biological structures. Generating an image requires serial acquisition of individual molecular positions at sufficient density to define a biological structure, increasing the acquisition time. Efficient analysis of biological structures from sparse localization data could substantially improve the dynamic imaging capabilities of these methods. Using a feature extraction technique called the Hough Transform simple biological structures are identified from both simulated and real localization data. We demonstrate that these generative models can efficiently infer biological structures in the data from far fewer localizations than are required for complete spatial sampling. Analysis at partial data densities revealed efficient recovery of clathrin vesicle size distributions and microtubule orientation angles with as little as 10% of the localization data. This approach significantly increases the temporal resolution for dynamic imaging and provides quantitatively useful biological information.

The Hough transform is a feature extraction technique used in image analysis, computer vision, and digital image processing.[1] The purpose of the technique is to find imperfect instances of objects within a certain class of shapes by a voting procedure. This voting procedure is carried out in a parameter space, from which object candidates are obtained as local maxima in a so-called accumulator space that is explicitly constructed by the algorithm for computing the Hough transform.

The classical Hough transform was concerned with the identification of lines in the image, but later the Hough transform has been extended to identifying positions of arbitrary shapes, most commonly circles or ellipses. The Hough transform as it is universally used today was invented by Richard Duda and Peter Hart in 1972, who called it a "generalized Hough transform"[2] after the related 1962 patent of Paul Hough.

- Draw on blackboard principle of Hough transform For lines

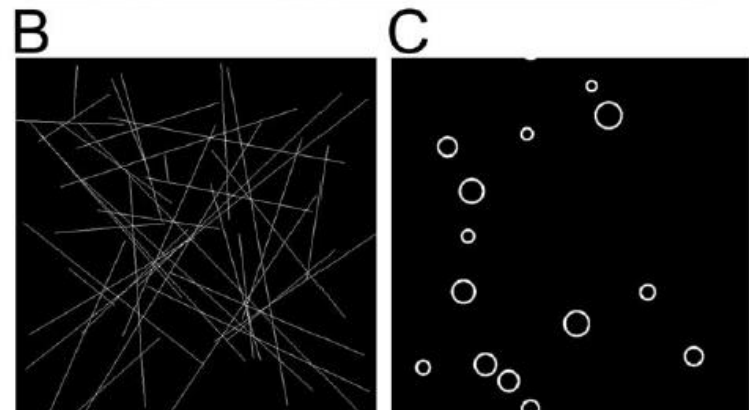
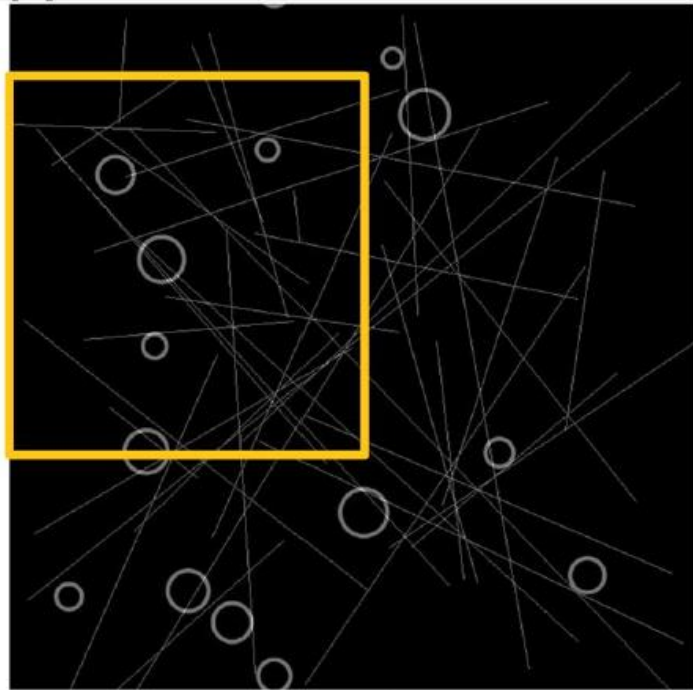


**Figure 1. Structural mask for simulated data.** (A) Lines and Circles, cropped image in the yellow rectangle box is shown in Figure 2. (B) lines only (C) circles only.

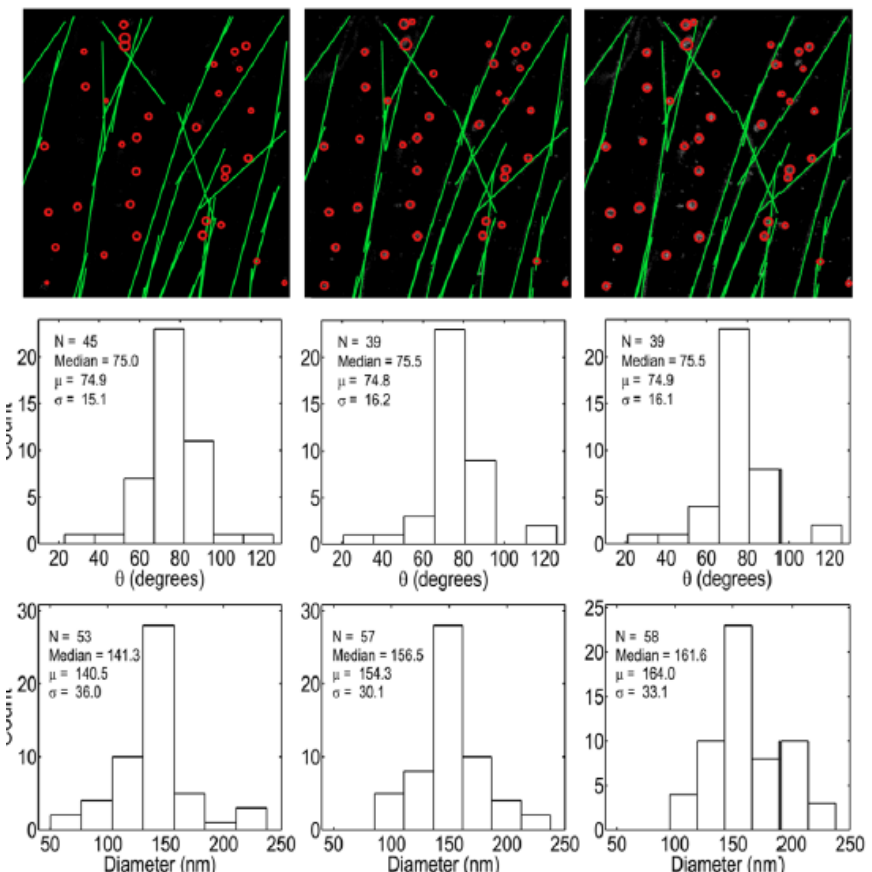
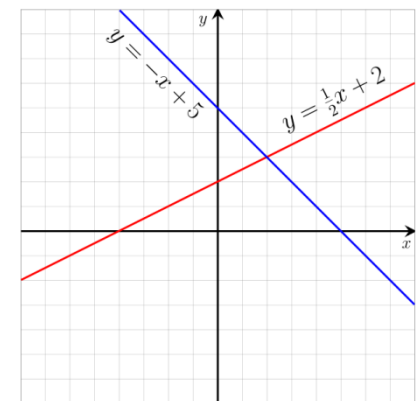
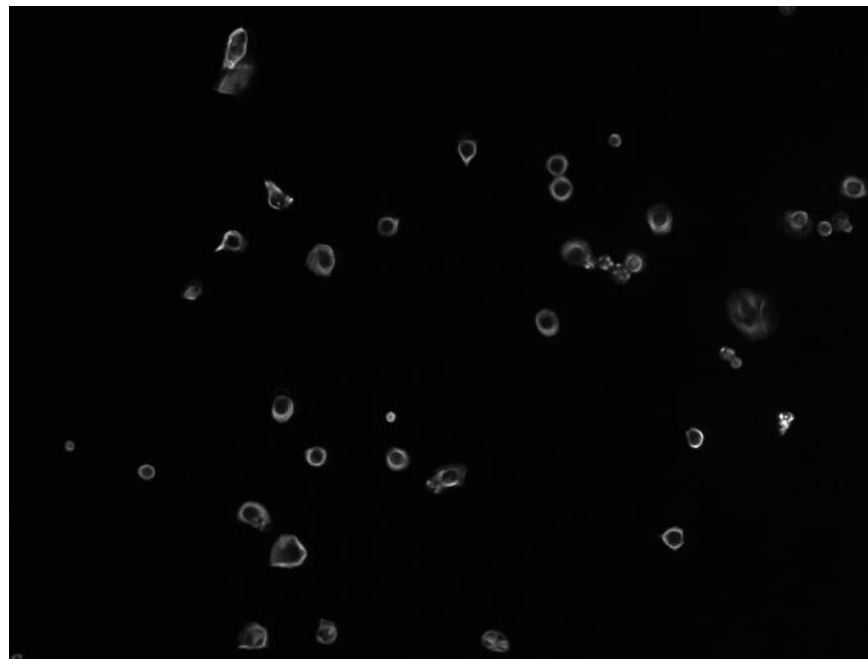


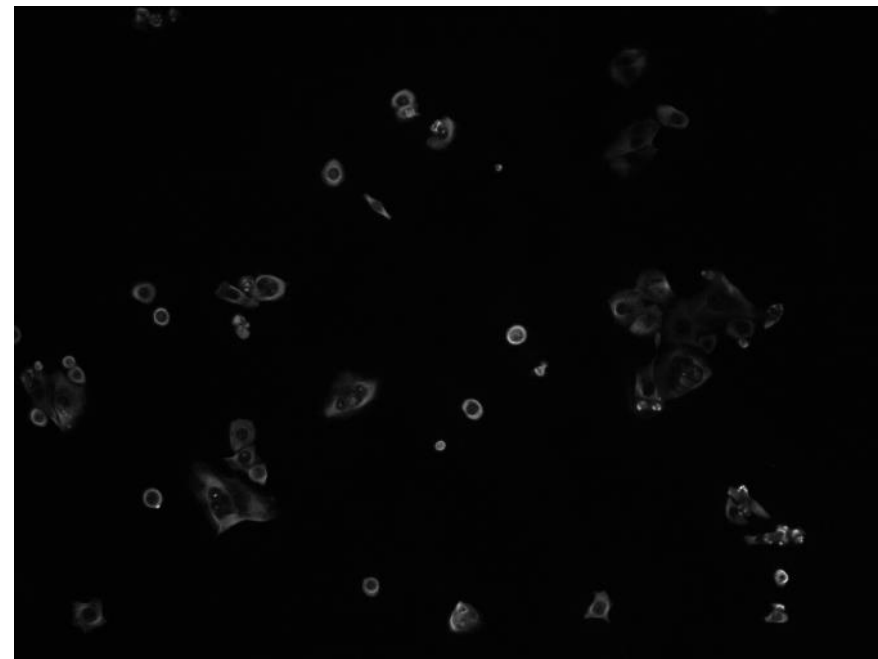
**Figure 5. Single molecule localized data of clathrin (red) and tubulin (green).** Top row is the plotter, second row is the representative reconstructed structures from both channels, overlaid on the 00% data. Third row is the histogram of orientation angle of the reconstructed line segments and the bottom row is the histogram of diameter.

## BRCA1 cells

- 1. Hough transform circle detection
- 2. Not only that there are more circles in A549, but the intensity of the circles in significantly higher



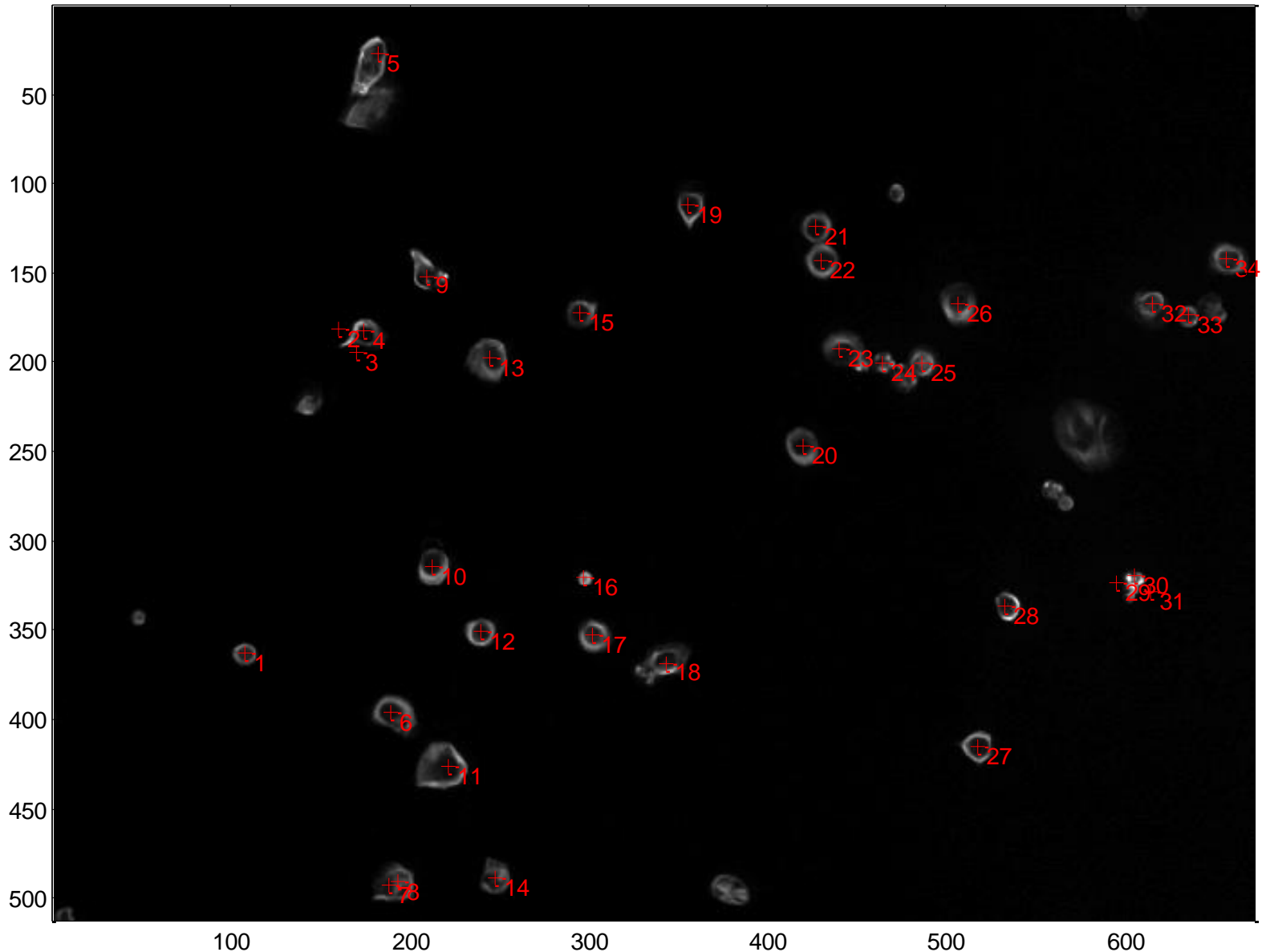
A549 PTX



B1KD PTX

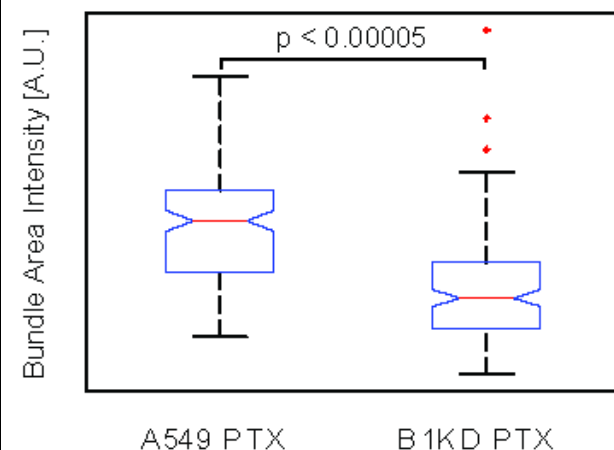
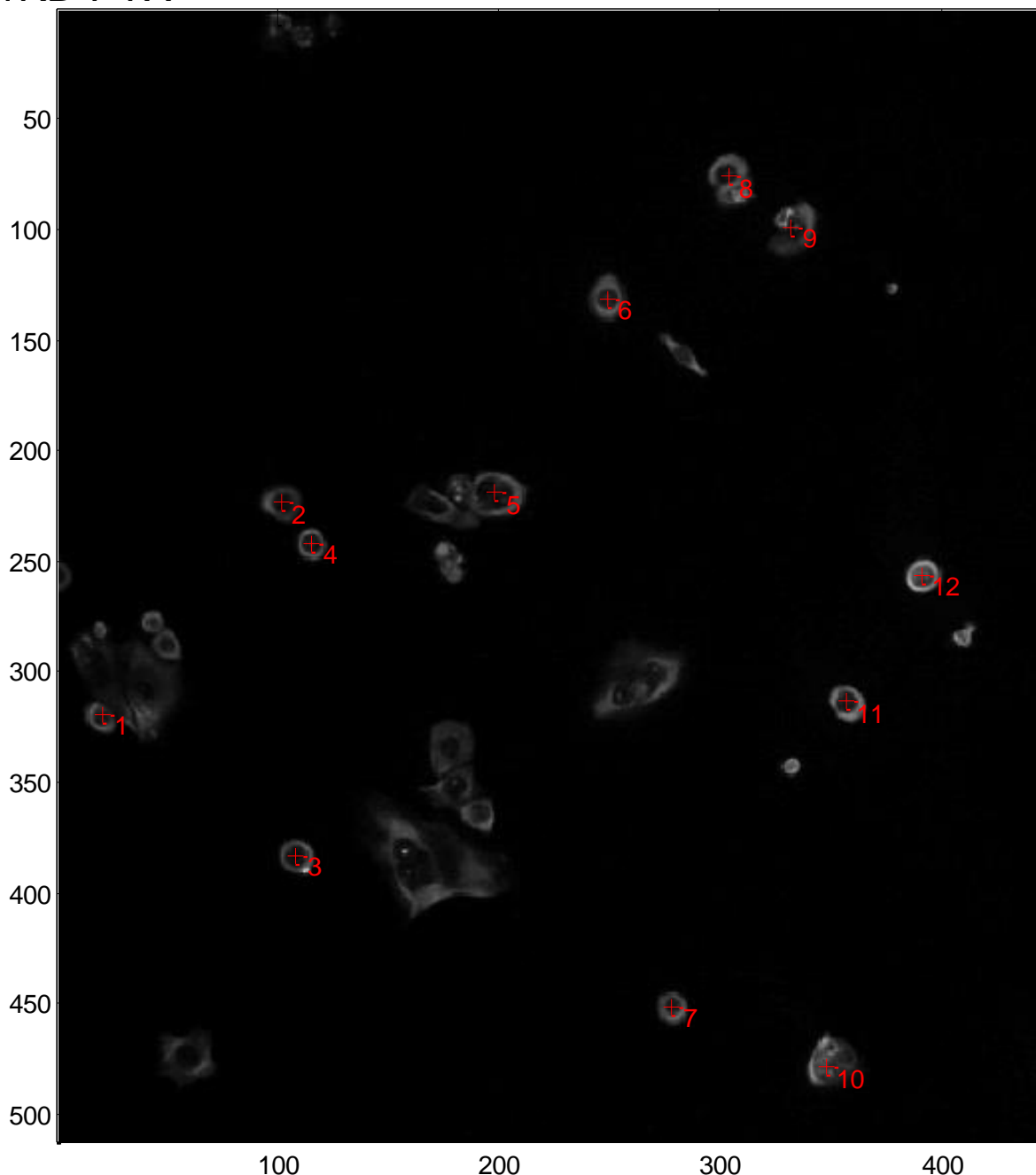
# A549 PTX

Raw Image TUB with Circles Detected (center positions marked)



B1KD PTX

Raw Image with Circles Detected (center positions marked)



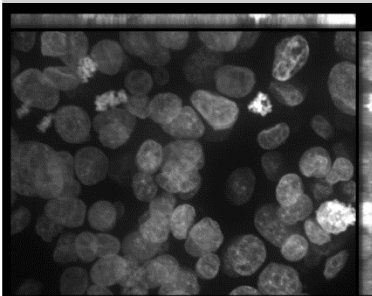
# analysis challenges

- in GC cells -> overlapping Dapi – so here I can not use the Voronoi diagram to split the image in cellular areas
- Solutions :
- 1. imaging sparser cells
- 2. adding a marker of cell outline
- 3. analysis “per field (images)” (we changed to that)
- 4. Segment DAPI areas (the problem here also is sometimes its multi-nuclei cells sometimes overlapping nuclei from different cells)

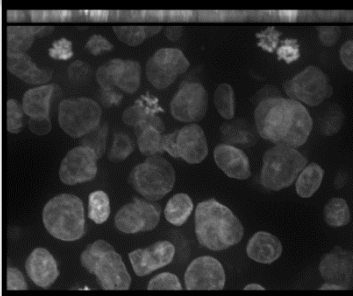
# Example GC groups of cells

- Task 1 – segment the DAPI areas - **find outline (SCH)**

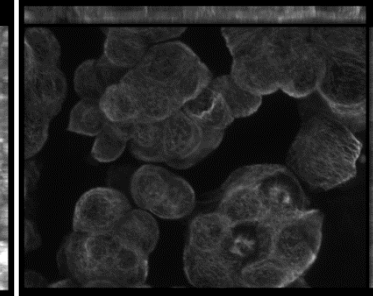
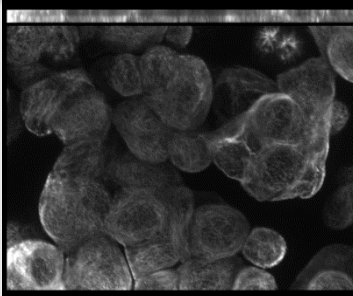
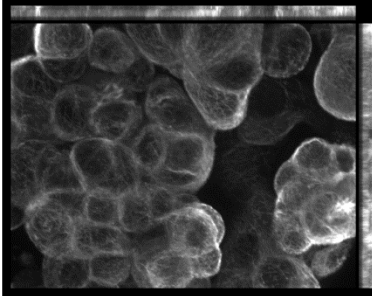
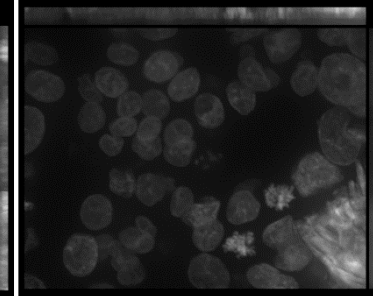
Untreated



Doc 10 nM



Doc 100 nM



# Improved Automatic Detection and Segmentation of Cell Nuclei in Histopathology Images

Yousef Al-Kofahi, Wiem Lassoued, William Lee, and Badrinath Roysam\*, *Senior Member, IEEE*

**Abstract**—Automatic segmentation of cell nuclei is an essential step in image cytometry and histometry. Despite substantial progress, there is a need to improve accuracy, speed, level of automation, and adaptability to new applications. This paper presents a robust and accurate novel method for segmenting cell nuclei using a combination of ideas. The image foreground is extracted automatically using a graph-cuts-based binarization. Next, nuclear seed points are detected by a novel method combining multiscale Laplacian-of-Gaussian filtering constrained by distance-map-based adaptive scale selection. These points are used to perform an initial segmentation that is refined using a second graph-cuts-based algorithm incorporating the method of alpha expansions and graph coloring to reduce computational complexity. Nuclear segmentation results were manually validated over 25 representative images (15 *in vitro* images and 10 *in vivo* images, containing more than 7400 nuclei) drawn from diverse cancer histopathology studies, and four types of segmentation errors were investigated. The overall accuracy of the proposed segmentation algorithm exceeded 86%. The accuracy was found to exceed 94% when only over- and undersegmentation errors were considered. The confounding image characteristics that led to most detection/segmentation errors were high cell density, high degree of clustering, poor image contrast and noisy background, damaged/irregular nuclei, and poor edge information. We present an efficient semiautomated approach to editing automated segmentation results that requires two mouse clicks per operation.

**Index Terms**—Image cytometry, cell nuclei, histopathology, segmentation.

interest in healthy and pathologic specimens [1], [2], and also for quantifying aspects of normal/diseased tissue architecture [1]. The cell nuclei may be stained using fluorescent markers [e.g., 4',6'-diamidino-2-phenylindole (DAPI)], or with histochemical stains (e.g., hematoxylin). It is important in these applications to be able to detect the correct number of cells with high accuracy, and to delineate them accurately with utmost automation and minimal human effort. It is also helpful to be able to easily adapt the software algorithms to images of different tissues captured under differing imaging conditions.

Automated segmentation of cell nuclei is now a well-studied topic for which a large number of algorithms have been described in the literature [2]–[18], and newer methods continue to be investigated. The main challenges in segmenting nuclei in histological, especially pathological tissue specimens, result from the fact that the specimen is a 2-D section of a 3-D tissue sample. The 2-D sectioning can result in partially imaged nuclei, sectioning of nuclei at odd angles, and damage due to the sectioning process. Furthermore, sections have finite thickness resulting in overlapping or partially superposed cells and nuclei in planar images. The end result of these limitations is a set of image objects that differ considerably from the ideal of round blob-like shapes. Their sizes and shapes in images can be irregular, and not always indicative of their 3-D reality. There is natural

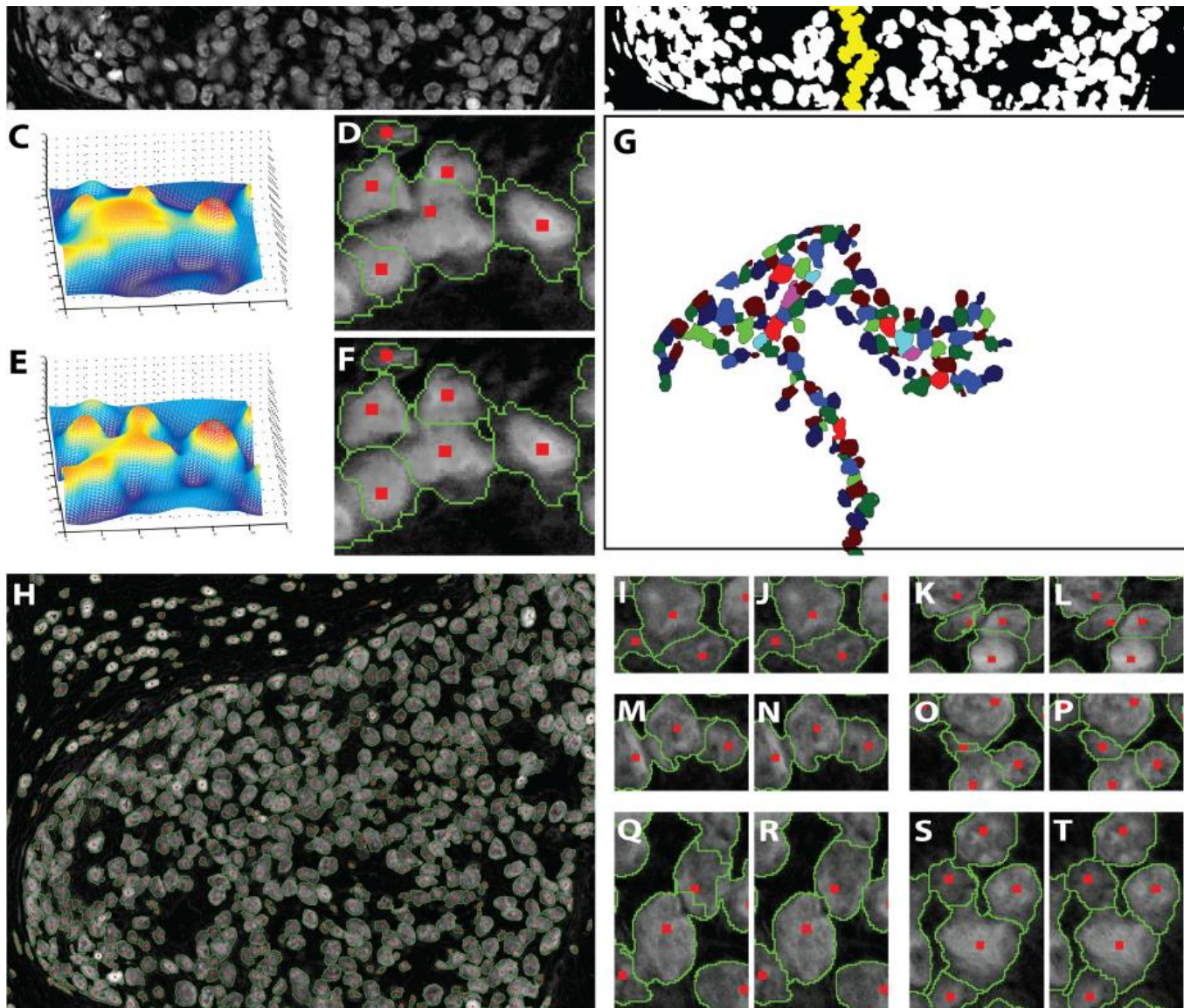


Fig. 2. Illustrating key steps of the proposed nuclear segmentation method. (A) Nuclear channel from spectral unmixing. (B) Foreground extraction results. Pixels marked yellow represent a large connected component. (C) Surface plot of the multiscale LoG filtering results for a small region. (D) Initial segmentation based on the LoG. (E) Surface plot of the distance-map-constrained multiscale LoG. (F) Improved initial segmentation resulting from the distance-constrained LoG. (G) Color coding of the yellow pixels in panel (B). (H) Final segmentation of the image in panel (A). Panels (I and J), (K and L), (M and N), (O and P), (Q and R), and (S and T) indicate initial and final segmentation closeups taken from different regions in the image shown in panel (H).

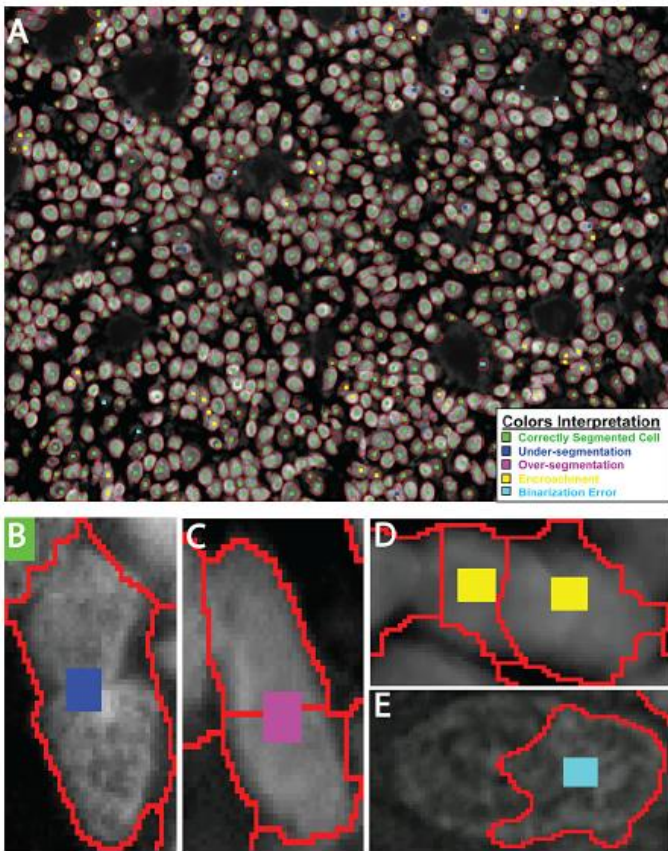


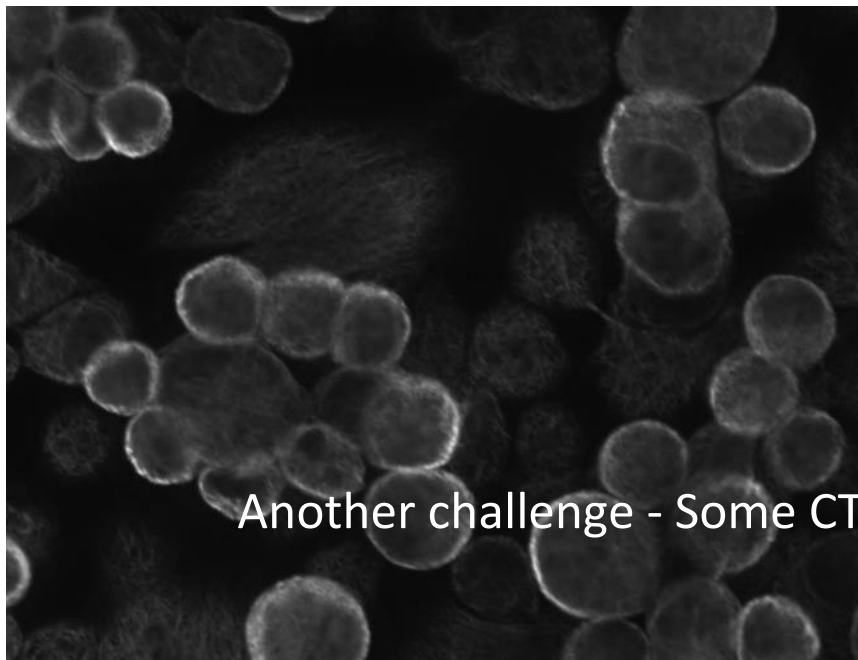
Fig. 5. Illustrating the results validation criteria. (A) Segmentation output of an image with color-coded seeds on each nucleus to identify whether it is correctly segmented or the type of segmentation error. (B) Example of an undersegmentation error. (C) Example of oversegmentation error. (D) Example of an encroachment error. (E) Example of a binarization error.

nuclei. The last type of segmentation errors is binarization er-

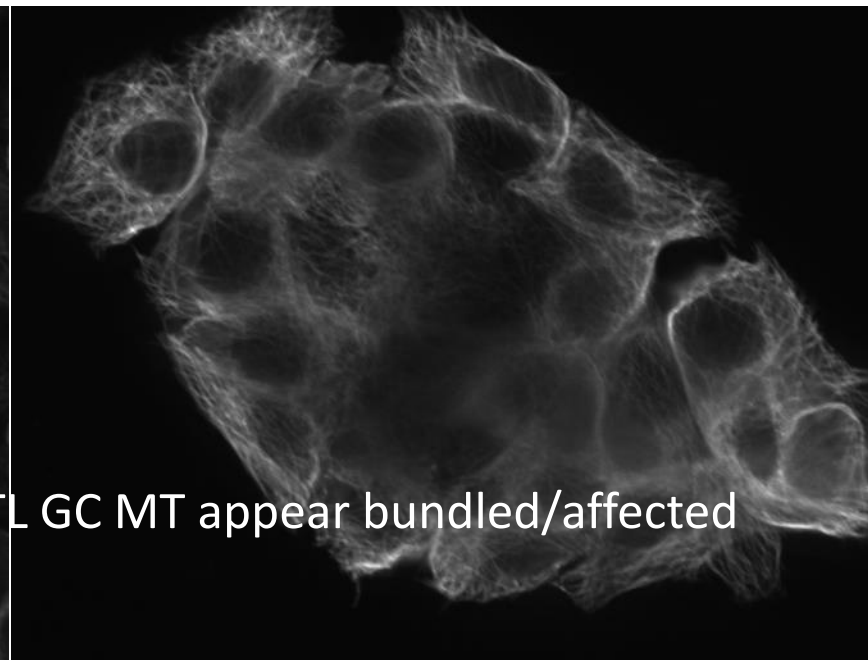
fully automated algorithm achieved  $>94\%$  accuracy. These data are helpful in comparing our algorithm to previously published methods [9], [18]. When encroachment and binarization errors are included, our algorithm showed an accuracy of more than 86%. The performance of our algorithm with regard to over- and undersegmentation errors can be described in terms of precision and recall measures. Specifically, the last two columns of these values are indicated in Table I. The overall  $F$ -measure ( $2 \times \text{precision} \times \text{recall}) / (\text{precision} + \text{recall})$ ) for these data is 0.97. We studied the performance of our binarization refinement step by comparing its output with the initial binarization using twenty 2-D phantom images for which we have ground truth data. For each image, we compared the percentages of incorrectly labeled pixels before and after binarization refinement using graph cuts, as detailed in Table II. Fig. 7(A) and (B) shows a sample phantom image and the corresponding ground truth. Initial segmentation output is shown in panel (C), while the refinement output is shown in panel (D). It is clear that significant improvement is achieved after applying graph-cuts refinement.

Finally, we studied the complexity reduction achieved using graph coloring by comparing segmentation processing times with and without graph coloring for 15 automatically created phantom images. All the images have the same size ( $300 \times 300$ ), with only one connected component (cluster of nuclei), and a varying number of nuclei in each cluster (10–150). Table III shows a summary of the analysis. Increasing numbers of nuclei in the cluster results in rapidly increasing processing time when graph coloring is not used. That is because the number of required  $\alpha$ -expansions is equal to the number of nuclei in the cluster. However, no significant increase in processing time is noted when graph coloring is used, since the number of

AGS CTL

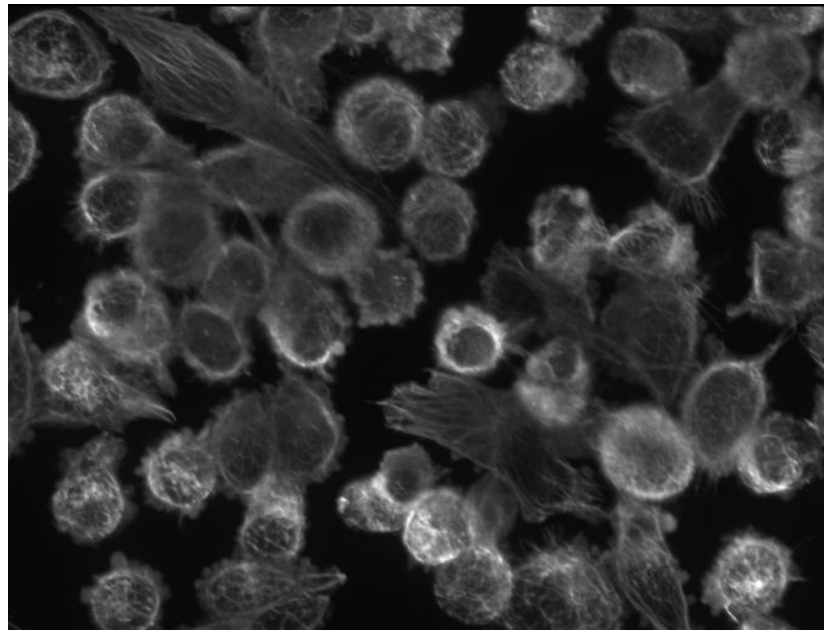


NCI-N87 CTL

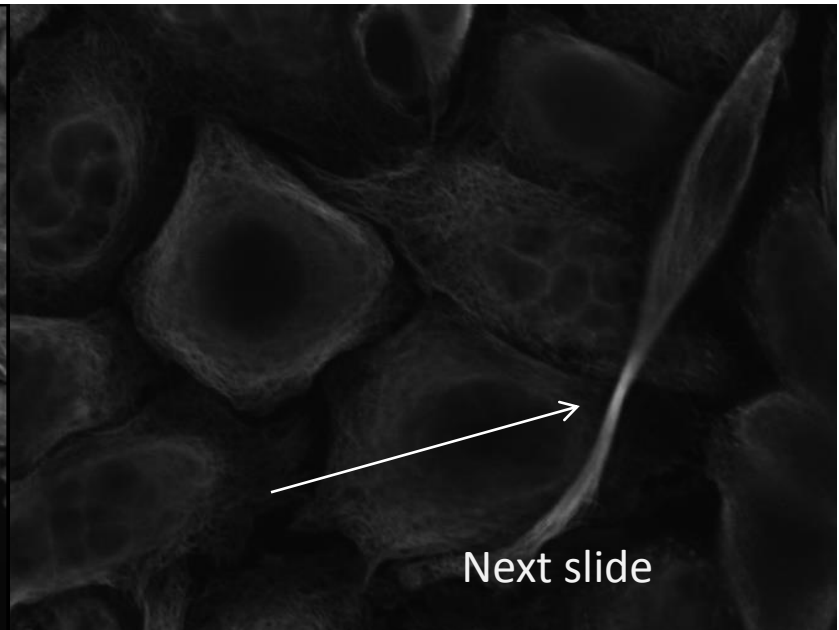


Another challenge - Some CTL GC MT appear bundled/affected

SNU1 CTL



MKN 7 10nM DTX



Next slide

# Combining Local Filtering and Multiscale Analysis for Edge, Ridge, and Curvilinear Objects Detection

Sylvain Berlemont, *Student Member, IEEE*, and Jean-Christophe Olivo-Marin, *Senior Member, IEEE*

**Abstract**—This paper presents a general method for detecting curvilinear structures, like filaments or edges, in noisy images. This method relies on a novel technique, the feature-adapted beamlet transform (FABT) which is the main contribution of this paper. It combines the well-known Beamlet transform (BT), introduced by Donoho *et al.*, with local filtering techniques in order to improve both detection performance and accuracy of the BT. Moreover, as the desired feature detector is chosen to belong to the class of steerable filters, our transform requires only  $O(N \log(N))$  operations, where  $N = n^2$  is the number of pixels. Besides providing a fast implementation of the FABT on discrete grids, we present a statistically controlled method for curvilinear objects detection. To extract significant objects, we propose an algorithm in four steps: 1) compute the FABT, 2) normalize beamlet coefficients, 3) select meaningful beamlets thanks to a fast energy-based minimization, and 4) link beamlets together in order to get a list of objects. We present an evaluation on both synthetic and real data, and demonstrate substantial improvements of our method over classical feature detectors.

**Index Terms**—Beamlet transform, curvilinear objects, edge, feature, Radon transform, ridge, statistical detection, steerable filters.

designed features. In the context of biological imaging, the diameter of structures such as microtubules or DNA molecules for instance is about 3 nm, which is far smaller than the point spread function (PSF) width of any standard microscope. Hence, it is acceptable to consider the transverse profile of such filaments to be approximated by a PSF model [46].

One way to detect curvilinear objects is to track locally the feature of the line profile; linear filtering or template matched filtering are well-known techniques for doing so. The classical Canny edge detector [14] is based on such linear filtering techniques. It involves the computation of correlations with shifted and/or rotated version of the feature template at every point in the image. Filtering is usually followed by a nonmaxima suppression and a thresholding step. These two processes yield a set of pixels which have to be linked together with a contour tracing algorithm. This final step may be tedious and has a high complexity [16].

Recently, optimized detectors have been proposed [35] that out-perform classical feature detectors like Canny edge detector or Hessian-based filter for ridge detection [25]. Authors define a

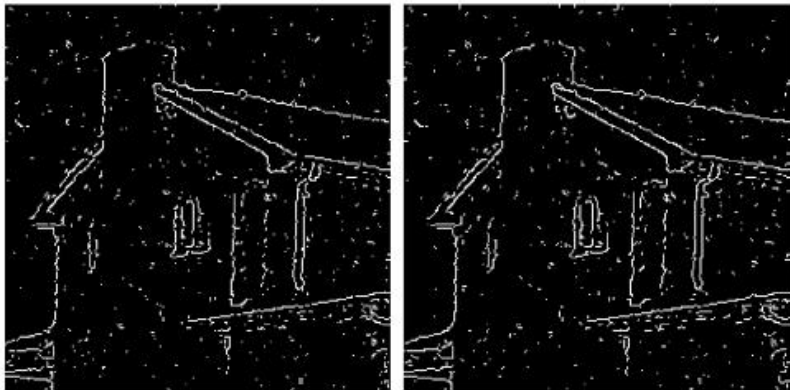


Fig. 10. Angular mean square error (radian) between maximum beamlet's orientation and the true orientation  $\theta$  of the line segment, in function of scale, computed over a set of 100 simulated images SNR =  $-5$ ,  $0$ , and  $5$  dB. Green bars correspond to FABT angular error, blue bars correspond to BT angular error.

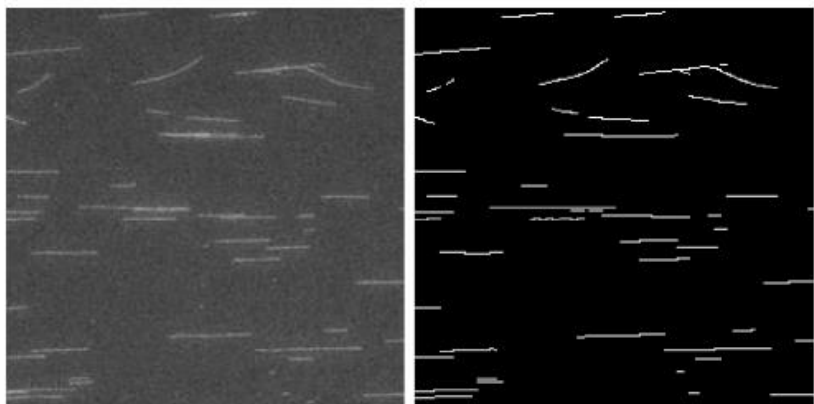


Fig. 11. Detection of  $\lambda$ -phage DNA molecules: original image (left), detection (right).

only. Our method is also able to retrieve features, for example most of the roof shadow lines, which are barely detected at pixel

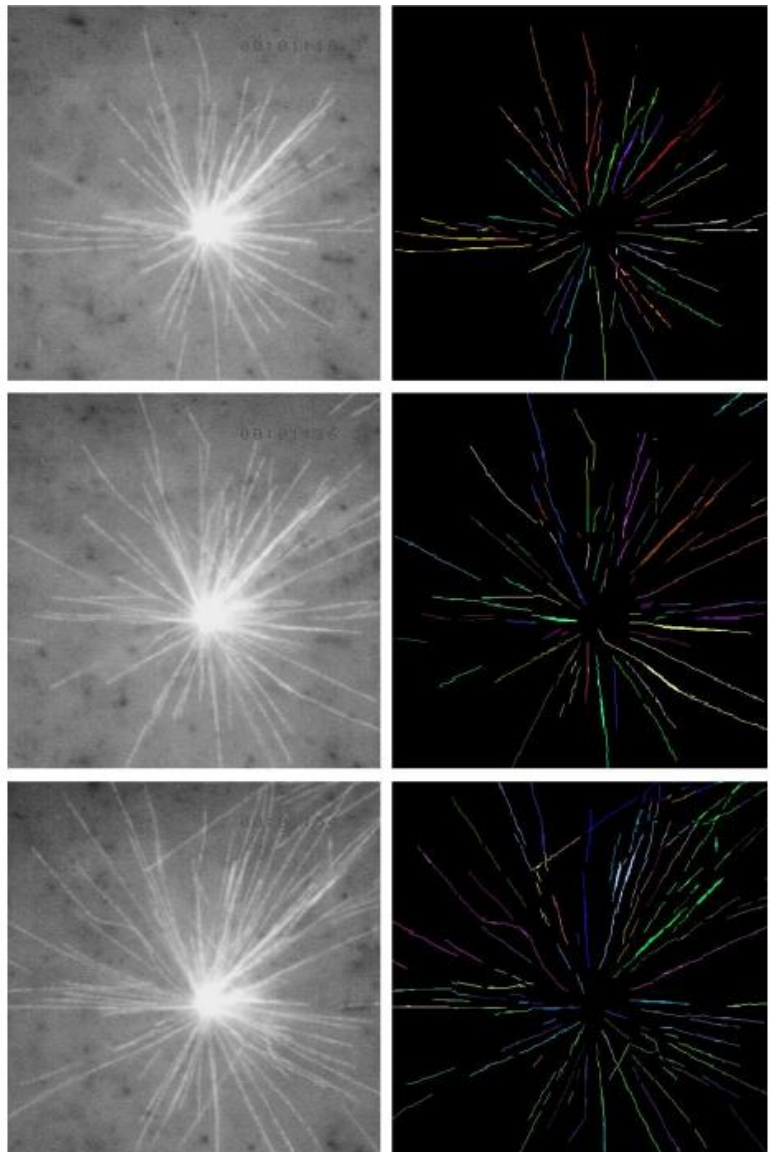


Fig. 12. Detection of full-length microtubules during interphase at  $t = 24$  s,  $32$ ,  $48$ , and  $76$  s. Right column shows the detection after chaining step. Each filament is labeled by a single color.

Dave Donoho - Home Page

www-stat.stanford.edu/~donoho/

# Dave Donoho

home . lectures . reports . software . students . courses . special



**David Donoho**  
**Statistics Department**  
**Stanford University**  
 Stanford, CA 94305, USA  
[donoho@stat.stanford.edu](mailto:donoho@stat.stanford.edu)  
 Voice: (650) 723-3350  
 Fax: (650) 725-8977

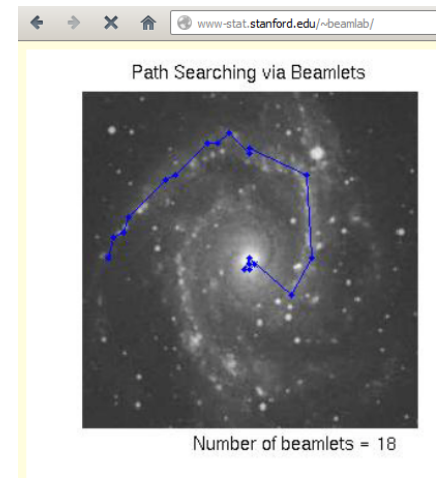


Winner of the  
 Open Directory  
 Cool Site award

The Research presented at this Web Site has been sponsored by National Science Foundation Grants DMS 92-09130, DMS-95-05151, DMS-98-72890, DMS-00-85984, DMS-00-72661, DMS-01-40540, and by other US Government Agencies.

[home](#) | [lectures](#) | [reports](#) | [software](#) | [students](#) | [courses](#) | [special](#)

- In mathematics, the Radon transform in two dimensions, named after the Austrian mathematician Johann Radon, is the integral transform consisting of the integral of a function over straight lines. The transform was introduced by Johann Radon (1917), who also provided a formula for the inverse transform. Radon further included formulas for the transform in three-dimensions, in which the integral is taken over planes. It was later generalised to higher-dimensional Euclidean spaces, and more broadly in the context of integral geometry. The complex analog of the Radon transform is known as the Penrose transform.



## BEAMLAB 200 for Matlab 5.x or 6.x

### Current Release

David Donoho  
 Ana Georgina Flesia  
 Xiaoming Huo  
 Ofer Levi

### Major Contributions from

Sou Cheng Choi  
 Danzhu Shi

### What is BeamLab?

BeamLab is a collection of Matlab functions that have been used by the authors and collaborators to implement a variety of computational algorithms related to beamlet, curvelet, ridgelet analysis. It includes about 900 Matlab files, datasets, and demonstration scripts. Some computationally expensive routines have been implemented as Matlab MEX functions.

### What is New?

For the new version (BeamLab200), we add in scripts to reproduce figures in recent papers by researchers from the Stanford Statistics Department (David L. Donoho) and their collaborators:

- D. Donoho and X. Huo, [Beamlets and Multiscale Image Processing](#), 2001 ↗
- A. Averbuch, R. Coifman, D. Donoho, M. Israeli and J. Walden, [Fast Slant Stack: A notion of Radon Transform for data on a Cartesian grid which is Rapidly Computable Algebraically Exact, Geometrically Faithful, and Invertible](#), 2001 ↗
- D. Donoho and A. Flesia, [Digital Ridgelet Transform Based on True Ridge Functions](#), 2002 ↗
- A. Flesia, H. Hel-Or, A. Averbuch, E. Candès, R. Coifman, D. Donoho, [Digital Implementation of Ridgelet Packets](#), 2002 ↗
- D. Donoho and O. Levi, [Fast X-Ray and Beamlet Transforms for Three-Dimensional Data](#), 2002 ↗
- D. Donoho and M. Duncan, [Digital Curvelet Transform: Strategy, Implementation and Experiments](#), 1999 ↗

The Radon transform is widely applicable to tomography, the creation of an image from the scattering data associated with cross-sectional scans of an object. If a function  $f$  represents an unknown density, then the Radon transform represents the scattering data obtained as the output of a tomographic scan. Hence the inverse of the Radon transform can be used to reconstruct the original density from the scattering data, and thus it forms the mathematical underpinning for tomographic reconstruction, also known as image reconstruction. The Radon transform data is often called a sinogram because the Radon transform of a Dirac delta function is a distribution supported on the graph of a sine wave. Consequently the Radon transform of a number of small objects appears graphically as a number of blurred sine waves with different amplitudes and phases. The Radon transform is useful in computed axial tomography (CAT scan), barcode scanners, electron microscopy of macromolecular assemblies like viruses and protein complexes, reflection seismology and in the solution of hyperbolic partial differential equations.

# Radon-Like Features and their Application to Connectomics

Ritwik Kumar<sup>1</sup>, Amelio Vázquez-Reina<sup>2</sup>, Hanspeter Pfister<sup>1</sup>

<sup>1</sup>School of Engineering and Applied Sciences, Harvard University, Cambridge, MA, USA

<sup>2</sup>Dept. of Computer Science, Tufts University, MA, USA,

{rkkumar, pfister}@seas.harvard.edu, amelio.vazquez-reina@tufts.edu

## Abstract

*In this paper we present a novel class of so-called Radon-Like features, which allow for aggregation of spatially distributed image statistics into compact feature descriptors. Radon-Like features, which can be efficiently computed, lend themselves for use with both supervised and unsupervised learning methods. Here we describe various instantiations of these features and demonstrate there usefulness in context of neural connectivity analysis, i.e. Connectomics, in electron micrographs. Through various experiments on simulated as well as real data we establish the efficacy of the proposed features in various tasks like cell membrane enhancement, mitochondria segmentation, cell background segmentation, and vesicle cluster detection as compared to various other state-of-the-art techniques.*

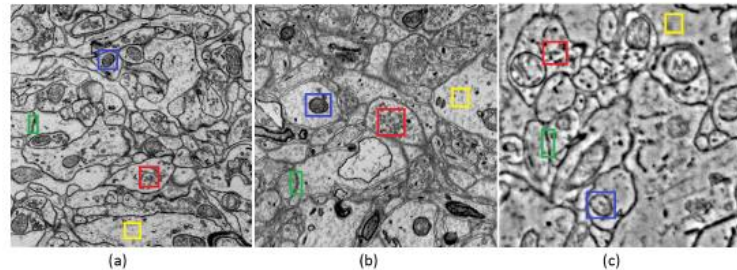


**Figure 1. Connectome Electron Microscopy Images:** The three different kind of images obtained as the staining process in the image acquisition pipeline is changed. Blue boxes show mitochondria, red boxes show vesicles, green boxes show cell boundaries and yellow boxes show cell background.

there are a large number of methods is because they are tailored, and rightly so, to work with a specific kind of images - Photographs, CT Scans, EM images etc. Primarily due to the novel nature of this data, the landscape of the im-

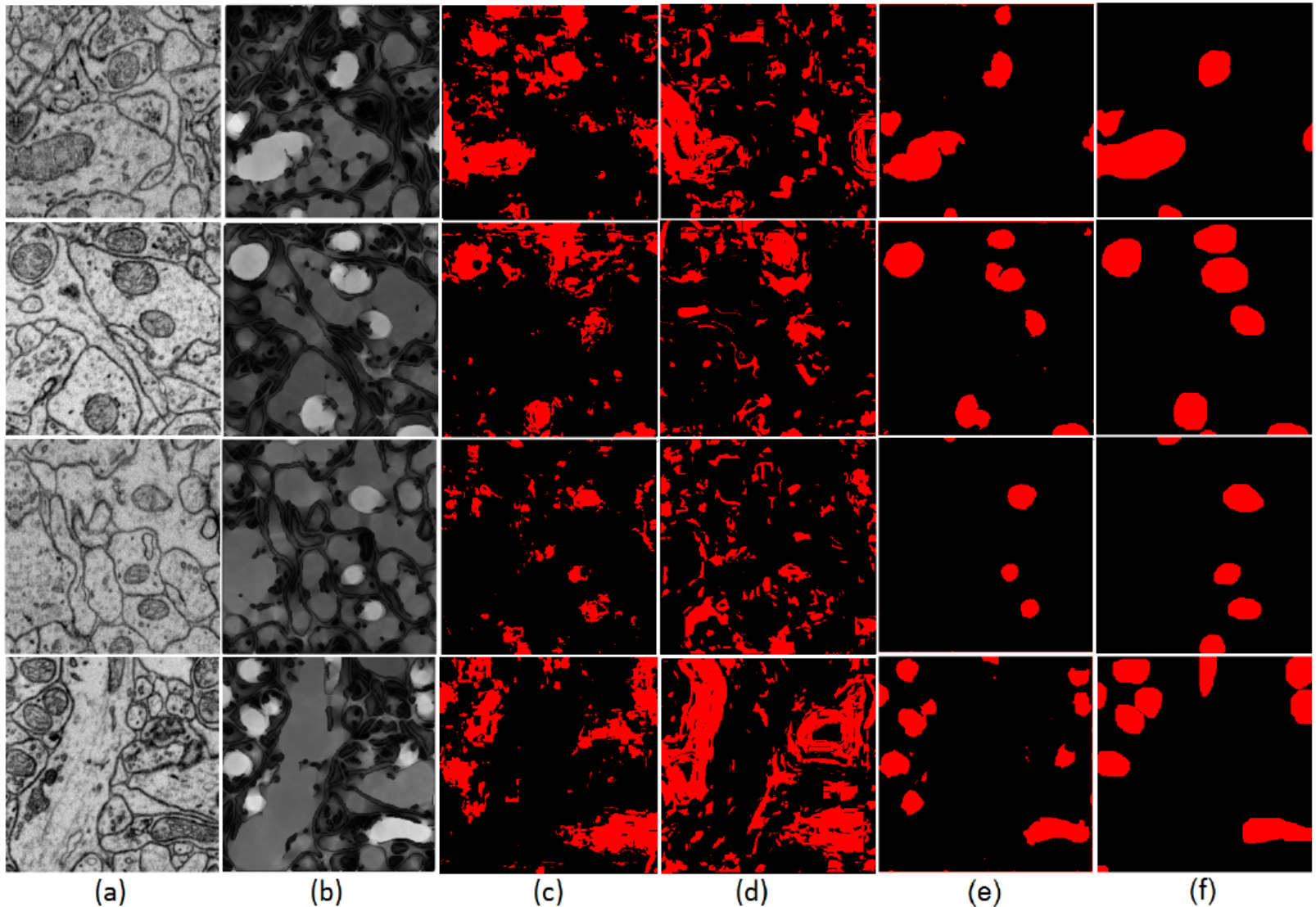


**Figure 8. Mitochondria Segmentation:** Column (a) shows  $512 \times 512$  input images and column (b) shows the pixel-wise mean of the obtained Radon-Like features (using the extraction function in Eq. 6). Column (c) presents results obtained using the texton-based Texture Classifier [14] and column (d) show results obtained using Gabor histogram features as suggested in [16]. Column (e) shows the segmentation obtained using Radon-Like features (thresholding (b)) and (f) shows the corresponding ground truth.

# Analysis “per field (image)”

IEEE TRANSACTIONS ON PATTERN ANALYSIS AND MACHINE INTELLIGENCE, VOL. 24, NO. 3, MARCH 2002

381

## Unsupervised Learning of Finite Mixture Models

Mario A.T. Figueiredo, *Senior Member, IEEE*, and Anil K. Jain, *Fellow, IEEE*

**Abstract**—This paper proposes an unsupervised algorithm for learning a finite mixture model from multivariate data. The adjective “unsupervised” is justified by two properties of the algorithm: 1) it is capable of selecting the number of components and 2) unlike the standard *expectation-maximization* (EM) algorithm, it does not require careful initialization. The proposed method also avoids another drawback of EM for mixture fitting: the possibility of convergence toward a singular estimate at the boundary of the parameter space. The novelty of our approach is that we do not use a model selection criterion to choose one among a set of preestimated candidate models; instead, we seamlessly integrate estimation and model selection in a single algorithm. Our technique can be applied to any type of parametric mixture model for which it is possible to write an EM algorithm; in this paper, we illustrate it with experiments involving Gaussian mixtures. These experiments testify for the good performance of our approach.

**Index Terms**—Finite mixtures, unsupervised learning, model selection, minimum message length criterion, Bayesian methods, expectation-maximization algorithm, clustering.

---

◆

---

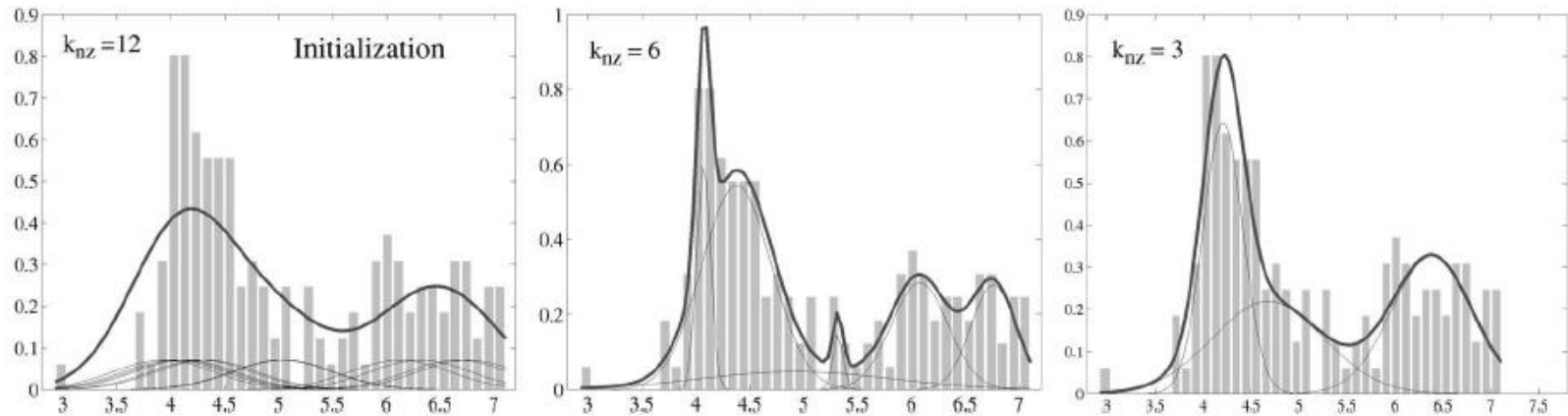


Fig. 7. Fitting a Gaussian mixture to the acidity data set. Our algorithm selects  $k_{nz} = 3$ .

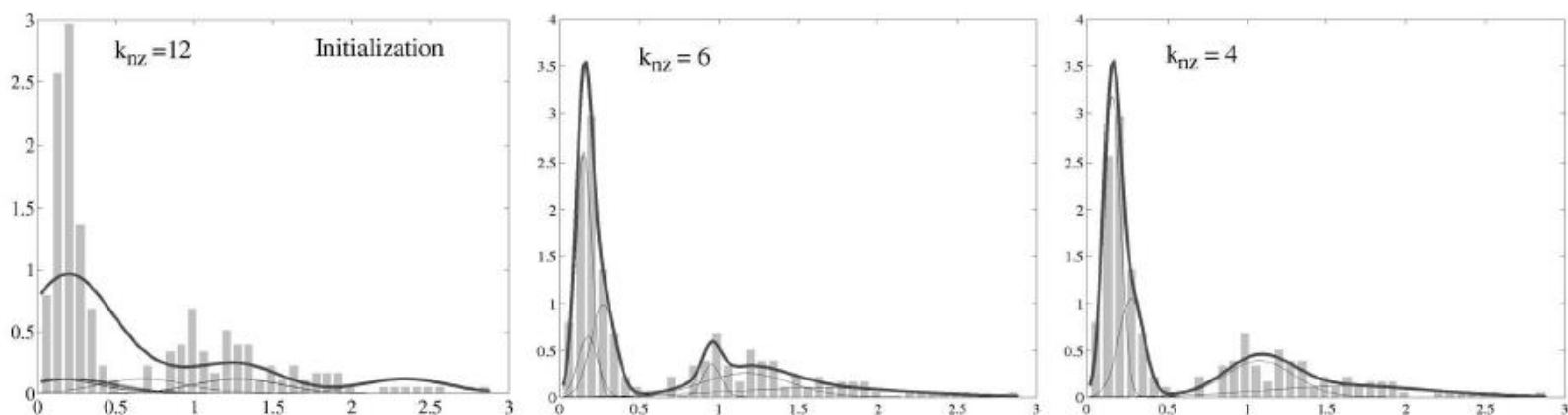


Fig. 8. Fitting a Gaussian mixture to the enzyme data set. Our algorithm selects  $k_{nz} = 4$ .

# Deformable Multi Template Matching with Application to Portal Images

Martin Berger and Gaudenz Danuser

Swiss Federal Institute of Technology

Communication Technology Lab, Image Science

8092 Zürich, Switzerland

{berger,danuser}@vision.ee.ethz.ch

## Abstract

*The exact positioning of patients during radiotherapy is essential for high precision treatment. The registration of portal image sequences can help to control the patient position. The particular problem of such megavoltage X-ray imagery is its extremely low contrast, rendering accurate feature extraction a difficult task. To circumvent the step of feature extraction, the algorithm presented in this paper relies on an area-based matching of the image signal using deformable templates. This strategy contrasts with most state of the art registration algorithms for portal imagery.*

*The paper includes the mathematical formalism of the least squares template matching method, as well as the framework for automated quality control, together yielding a fast, robust and very accurate image matching procedure. Tests on 17 portal image series with more than 100 images in total have shown very satisfying results. Artificially rotated and shifted images demonstrate the performance of the method with respect to a ground truth.*

thermore, most state of the art techniques require too much user interaction. Algorithms like point-to-point (or landmark) matching greatly depend on the exact localization of the landmarks by the physician. This is not only time-consuming, but also varies for different operators. Less user interaction is required by the chamfer matching algorithm where significant ridges are manually outlined in a reference image and matched onto the detected features of the treatment image [8]. A similar approach in the sense that it also uses binary features, namely cores, is described in [7], where also a quite complete review about published algorithms for portal imaging can be found.

Since portal images are inherently noisy and low in contrast, it is difficult to robustly detect features like edges, ridges or cores. Therefore, an area-based match is superior to a feature-based algorithm. Greyvalue correlation techniques are described in [6, 12, 13]. Their limitations lie in the restriction to a translation or in a coarse search grid for computational reasons.

A distinct approach has been proposed in [2]. Based on

	dx [mm]	dy [mm]	rot [deg]
original	-0.08	-6.88	0.05
rotated (ground truth)	-1.85	-6.63	-14.95
rotated (estimated)	-1.86	-6.63	-14.95

**Table 1. Consistency test of field edge displacement with respect to a ground truth.**

12 mm translation and 4.5° rotation, which is reasonable as an upper limit for alignment errors in daily hospital routine.

The matching results are validated by visual inspection using combined cursors and verification lines. For all but one AP pelvis image the algorithm finds the correct displacement, *i.e.*, there are no visually noticeable errors. In two cases, the correct displacement is achieved after the manual exclusion or redefinition of a template. All others yield robust matches with a set of unoptimized templates. An example for a successful match is shown in figures 3 and 4.

Lateral pelvis fields are inherently more difficult to match. Still, from 25 images, only five pose problems in the sense that the templates had to be manually adjusted once. Two images needed more than one attempt. Figures 5 and 6 illustrate the potential of LSM. Even on this low-contrast and blurred imagery, a stable transformation is found.

In any case where an incorrect displacement is estimated, a low correlation value reliably indicates the mismatch.

## 5. Discussion and outlook

This work presents a novel application of least squares matching to portal images. The major difference between LSM and existing algorithms for portal imaging is the area-based matching approach in contrast to feature-based methods. The inherently low-contrast and noisy portal images pose problems on robust feature extraction, which is circumvented in this algorithm. Apart from avoiding the extraction of binary features, the area-based matching has the

o degrees to test the iterative matching process.

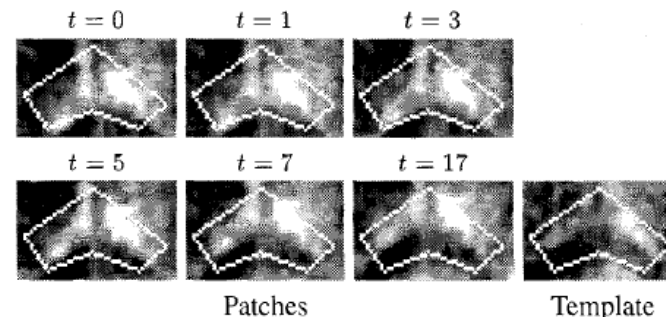


**Figure 4. Iteration series of the middle template in the above pelvis image. Notice that the contrast is manually enhanced for printing purpose.**

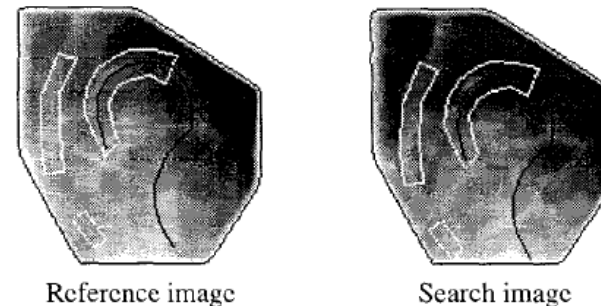


**Figure 5. Anatomy match example of an lateral pelvis image. The resulting translation is (2.4 mm, -3.8 mm) and the rotation 1.7 degrees.**

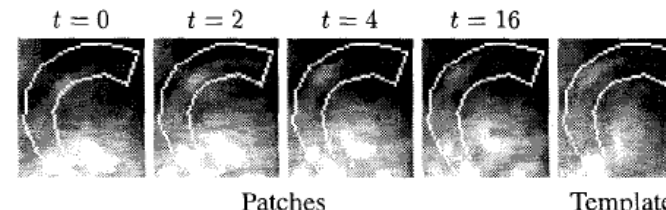


**Figure 6. Iteration series of the lateral pelvis image shown in figure 5.**

# Detection of meibomian glands and classification of meibography images

Yang Wei Koh,<sup>a</sup> Turgay Celik,<sup>a</sup> Hwee Kuan Lee,<sup>a</sup> Andrea Petznick,<sup>b</sup> and Louis Tong<sup>b,c,d,e</sup>

<sup>a</sup>Bioinformatics Institute, 30 Biopolis Street, 07-01, Matrix, Singapore 138671

<sup>b</sup>Singapore Eye Research Institute, 11, Third Hospital Avenue, Singapore 168751

<sup>c</sup>Singapore National Eye Center, 11, Third Hospital Avenue, Singapore 168751

<sup>d</sup>Duke National University of Singapore, Graduate Medical School, 8 College Road, Singapore 169857

<sup>e</sup>National University of Singapore, Yong Loo Lin School of Medicine, 1E Kent Ridge Road, Singapore 119228

**Abstract.** Computational methods are presented that can automatically detect the length and width of meibomian glands imaged by infrared meibography without requiring any input from the user. The images are then automatically classified. The length of the glands are detected by first normalizing the pixel intensity, extracting stationary points, and then applying morphological operations. Gland widths are detected using scale invariant feature transform and analyzed using Shannon entropy. Features based on the gland lengths and widths are then used to train a linear classifier to accurately differentiate between healthy (specificity 96.1%) and unhealthy (sensitivity 97.9%) meibography images. The user-free computational method is fast, does not suffer from inter-observer variability, and can be useful in clinical studies where large number of images needs to be analyzed efficiently. © 2012 Society of Photo-Optical Instrumentation Engineers (SPIE). [DOI: [10.1117/1.JBO.17.8.086008](https://doi.org/10.1117/1.JBO.17.8.086008)]

Keywords: dry-eye; meibography; diagnosis; computer vision; image processing; machine learning.

Paper 12259 received Apr. 27, 2012; revised manuscript received Jul. 18, 2012; accepted for publication Jul. 20, 2012; published online Aug. 8, 2012.

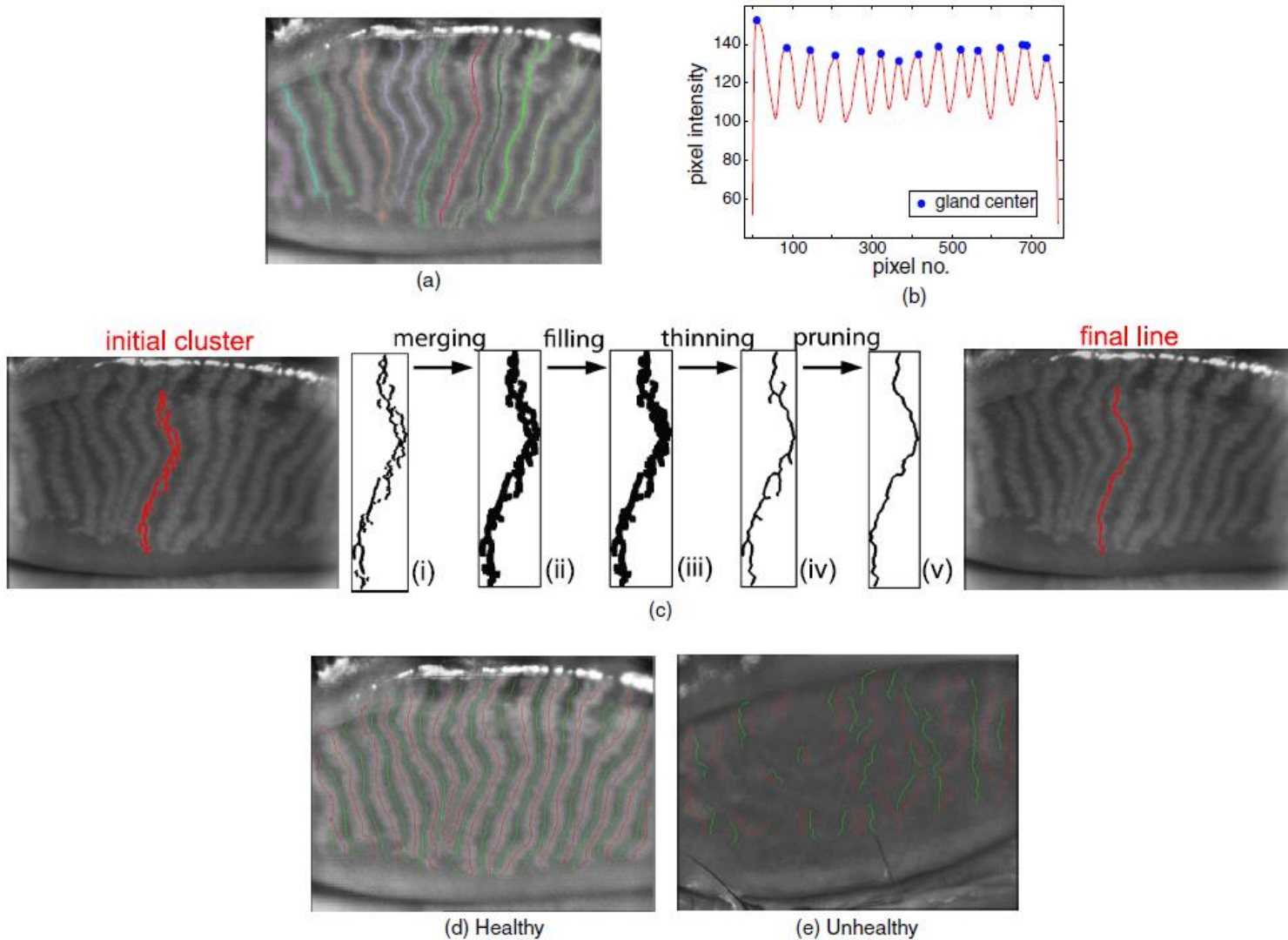


**Fig. 1** Extracting gland and inter-gland lines. (a) Lines along the centers of the glands can be located by computing the local maxima. The maxima are separated into the shown colored groups using a clustering algorithm. (b) Pixel intensity profile (after Gaussian smoothing) for one row of the image shown in (a). Gland centers are located at the local maxima. (c) Steps to process a cluster of local maxima points into a continuous curve. (d) and (e) The gland (red) and inter-glands (green) lines obtained for a healthy and an unhealthy image.

# SUPPORT VECTOR MACHINE LEARNING FOR DETECTION OF MICROCALCIFICATIONS IN MAMMOGRAMS<sup>1</sup>

*Issam El-Naqa, Yongyi Yang, Miles N. Wernick, Nikolas P. Galatsanos, and Robert Nishikawa\**

Dept. of Electrical and Computer Engineering, Illinois Institute of Technology  
3301 S. Dearborn Street, Chicago, IL 60616

\*Department of Radiology, University of Chicago  
5841 South Maryland Avenue, Chicago, IL 60637

## ABSTRACT

*Microcalcification (MC) clusters in mammograms can be an indicator of breast cancer. In this work we propose for the first time the use of support vector machine (SVM) learning for automated detection of MCs in digitized mammograms. In the proposed framework, MC detection is formulated as a supervised-learning problem and the method of SVM is employed to develop the detection algorithm. The proposed method is developed and evaluated using a database of 76 mammograms containing 1120 MCs. To evaluate detection performance, free-response receiver operating characteristic (FROC) curves are used. Experimental results demonstrate that, when compared to several other existing methods, the proposed SVM framework offers the best performance.*

modeling was proposed in [10]. A method based on “region growing” and active contours was studied in [11]. More recently, a two-stage neural network approach was proposed in [12].

In this work we investigate for the first time the use of a support vector machine (SVM) learning framework for MC detection, and show that it provides the best performance among the methods we have tested so far. SVM learning is based on the principle of structural risk minimization [13]. Instead of directly minimizing learning error, it aims to minimize the bound on the generalization error. As a result, an SVM is able to perform well when applied to data outside the training set. In recent years SVM learning has been applied to a wide range of real-world applications where it has been found to offer superior performance to that of competing methods [14].

In the proposed work, MC detection is considered as a

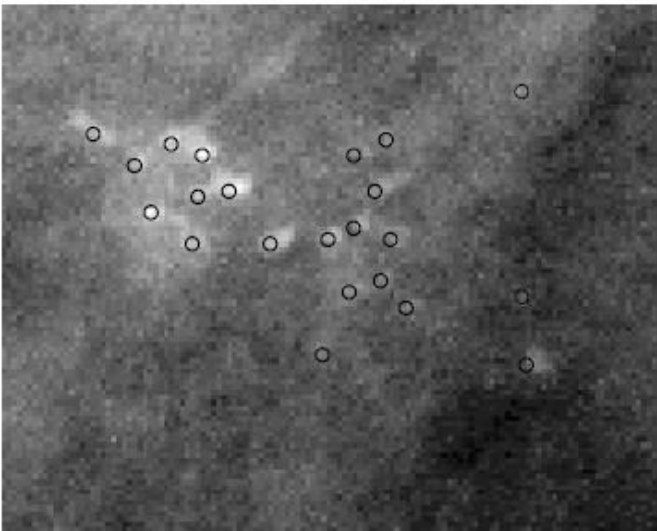


**Figure 1.** A section of a mammogram containing multiple MCs (labeled with circles).

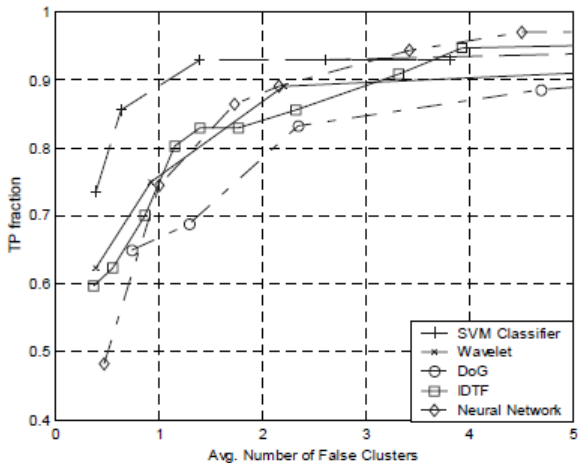


**Figure 4.** FROC curves obtained for the different methods evaluated. A higher FROC curve indicates better performance. The most significant portion of the curves is at the low end of the number of false positive clusters, where one would prefer to operate.

**Issam El Naqa**

Associate Professor

Oncology

**Address:**

Medical Physics  
Montreal General Hospital  
Room #L5-112  
1650 Cedar Avenue  
Montreal, QC H3G 1A4



**Telephone:** 514-934-1934, x45302

**E-mail:** [issam.elnaqa@mcgill.ca](mailto:issam.elnaqa@mcgill.ca)

**Education:** PhD., Illinois Institute of Technology; M.A. (Biology), Washington University

**Research Focus:** Oncology Informatics, Computational and System Biology, Image-guided and Adaptive Radiotherapy

# An active role for machine learning in drug development

Robert F Murphy

Because of the complexity of biological systems, cutting-edge machine-learning methods will be critical for future drug development. In particular, machine-vision methods to extract detailed information from imaging assays and active-learning methods to guide experimentation will be required to overcome the dimensionality problem in drug development.

High-throughput and high-content screening have been widely adopted by pharmaceutical and biotechnology companies as well as by many academic labs over the past 20 years, with the goal of rapidly identifying potential drugs that affect specific molecular targets<sup>1–3</sup>. These technologies dramatically enhance the rate and amount of information that can be collected about the effects of chemical compounds, and publicly funded efforts such as the Molecular Libraries Screening Centers of the US National Institutes of Health have permitted the creation of extensive databases such as PubChem. These databases typically contain the results of many screens in the form of scores for many compounds on a given assay, and they also contain information on the structures of compounds and the targets of particular assays. However, the premise that effective drugs can be found by screening primarily in single-target assays has run aground on the complex network of interactions

models, is well suited to address. Thus, machine learning will have an increasingly important role in the drug discovery and development process in the future. Here I focus on two areas where machine learning can have a profound impact: the use of machine-vision methods to improve information extraction from high-content assays and the use of active machine learning to drive experimentation.

## Seeing more in an assay

High-throughput microscopy and high-content screening are widely used to determine the effects of small-molecule compounds, inhibitory RNAs or other treatments (collectively referred to as perturbagens) on both specific molecular targets and cell behaviors. Analysis for high-content screens is typically done by calculating features that describe aspects of the images and training a classifier (Fig. 1a, i) to recognize the expected patterns (for example, of positive and negative controls)<sup>6,7</sup>.

cannot be used for more than one cell type. This not only requires retraining for each cell type but, more importantly, also does not readily allow comparison of patterns between cell types.

Machine-vision methods have the potential to extract more detailed information from high-content assays than methods currently in use. Pattern-unmixing methods seek to address the continuous nature of relocation events by estimating the fraction of a target that is in each of the subcellular locations. This can be done by both supervised methods (Fig. 1a, ii), in which the locations are specified, and unsupervised methods (Fig. 1a, iii), in which the patterns are discovered at the same time that the fractions are estimated. Once discovered, the patterns can be represented by learning-generative models (Fig. 1a, iv), as discussed below.

In addition to their role in drug development, perturbagen studies also improve our understanding of cellular

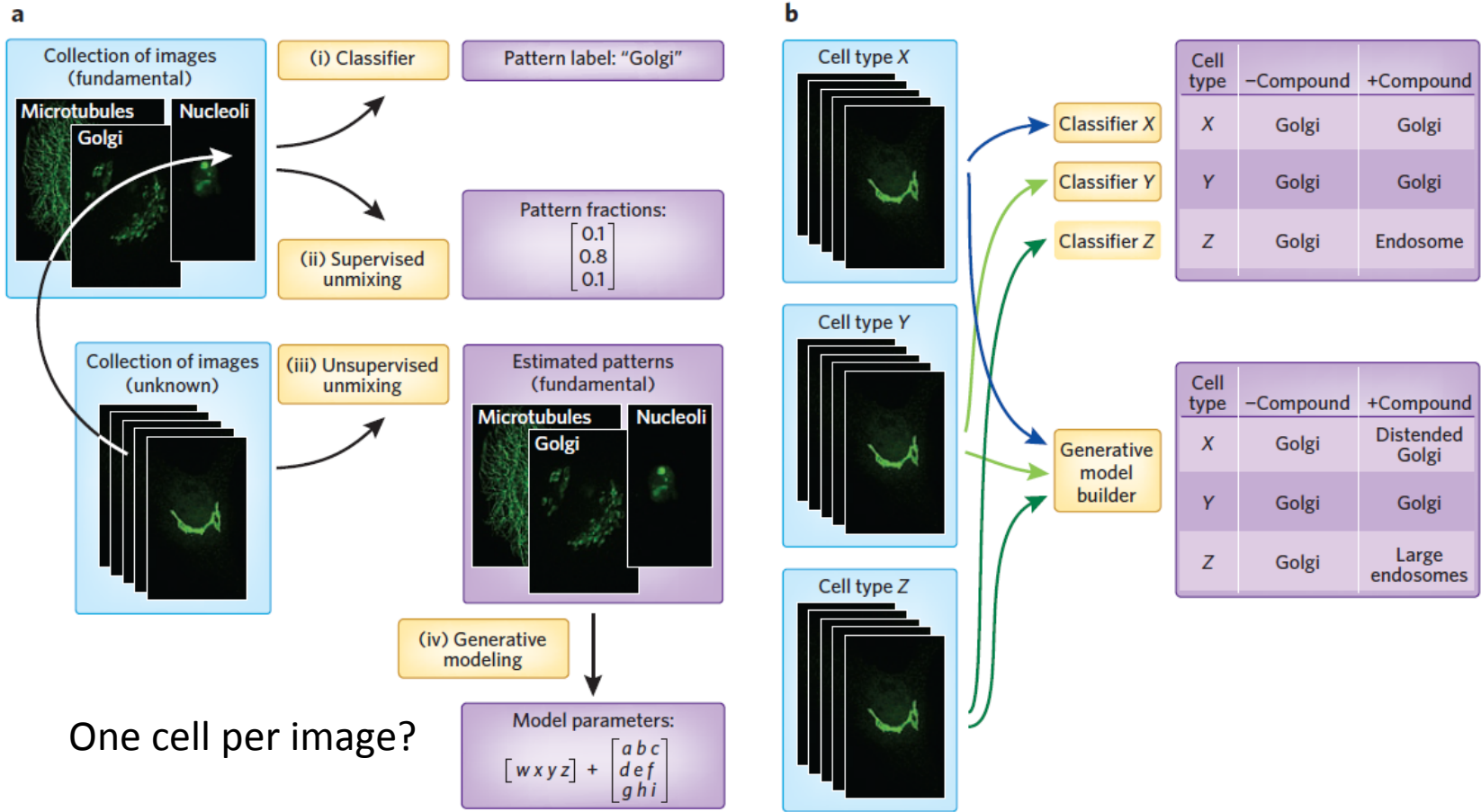
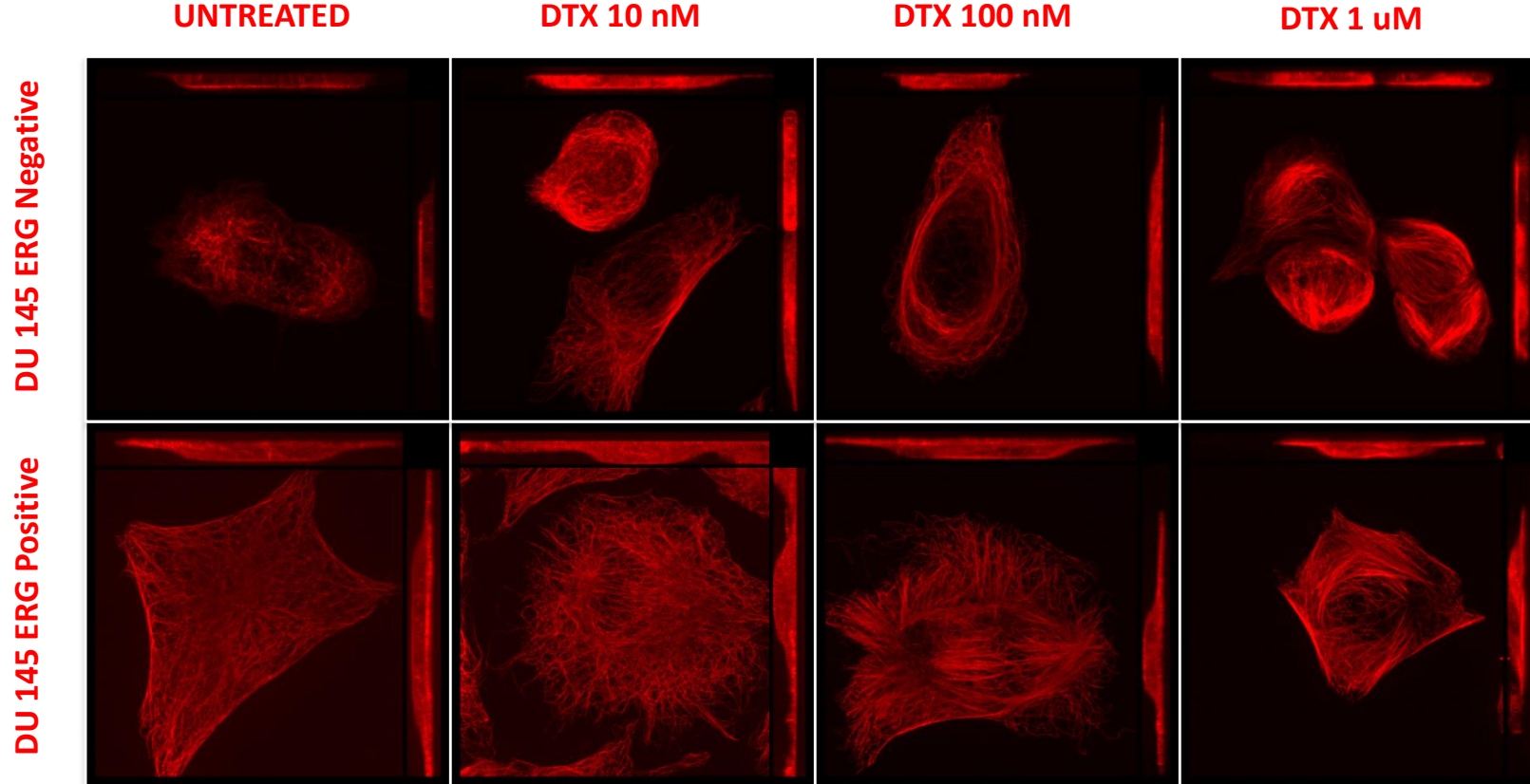


**Figure 1 |** Machine-vision methods for identifying and resolving drug and disease effects on protein distributions. **(a, i)** Given a collection of images for a cell type with unknown patterns (such as tagged proteins with unknown subcellular distributions) and images for proteins with known (fundamental) location patterns in that cell type, a classifier can be trained to recognize those subcellular patterns and used to assign a label to each unknown image. If the unknown images contain a mixture of patterns, results will be unpredictable. **(a, ii)** As an alternative, the fundamental location images can be used to train a supervised pattern-unmixing system so that the fraction of each unknown protein present in each fundamental pattern can be determined. This provides a better representation for the protein's distribution. **(a, iii)** If images of the fundamental patterns are not available (or if all patterns are not known), unsupervised pattern unmixing can be used to simultaneously estimate the fundamental patterns and the fraction in each. **(a, iv)** Lastly, the fundamental patterns can each be represented

**Table 1** Feature sets defined for 2-D fluorescence microscope images.

Set	SLF number	Feature description
SLF1	SLF1.1	The number of fluorescence objects in the image
	SLF1.2	The Euler number of the image (no. of holes minus no. of objects)
	SLF1.3	The average number of above-threshold pixels per object
	SLF1.4	The variance of the number of above-threshold pixels per object
	SLF1.5	The ratio of the size of the largest object to the smallest
	SLF1.6	The average object distance to the cellular center of fluorescence (COF)
	SLF1.7	The variance of object distances from the COF
	SLF1.8	The ratio of the largest to the smallest object to COF distance
	SLF1.9	The fraction of the nonzero pixels that are along an edge
	SLF1.10	Measure of edge gradient intensity homogeneity
	SLF1.11	Measure of edge direction homogeneity 1
	SLF1.12	Measure of edge direction homogeneity 2
	SLF1.13	Measure of edge direction difference
	SLF1.14	The fraction of the convex hull area occupied by protein fluorescence
	SLF1.15	The roundness of the convex hull
	SLF1.16	The eccentricity of the convex hull
SLF2	SLF2.1 to 2.16	SLF1.1 to SLF1.16
	SLF2.17	The average object distance from the COF of the DNA image
	SLF2.18	The variance of object distances from the DNA COF
	SLF2.19	The ratio of the largest to the smallest object to DNA COF distance
	SLF2.20	The distance between the protein COF and the DNA COF
	SLF2.21	The ratio of the area occupied by protein to that occupied by DNA
	SLF2.22	The fraction of the protein fluorescence that co-localizes with DNA
SLF3	SLF3.1 to 3.16	SLF1.1 to SLF1.16
	SLF3.17 to 3.65	Zernike moment features
	SLF3.66 to 3.78	Haralick texture features
SLF4	SLF4.1 to 4.22	SLF2.1 to 2.22
	SLF4.23 to 4.84	SLF3.17 to 3.78
SLF5	SLF5.1 to SLF5.37	37 features selected from SLF4 using stepwise discriminant analysis
SLF6	SLF6.1 to 6.65	SLF3.1 to SLF3.65
SLF7	SLF7.1 to 7.9	SLF3.1 to 3.9
	SLF7.10 to 7.13	Minor corrections to SLF3.10 to SLF3.13
	SLF7.14 to 7.65	SLF3.14 to SLF3.65
	SLF7.66 to 7.78	Haralick texture features calculated on fixed size and intensity scales
	SLF7.79	The fraction of cellular fluorescence not included in objects
	SLF7.80	The average length of the morphological skeleton of objects
	SLF7.81	The average ratio of object skeleton length to the area of the convex hull of the skeleton
	SLF7.82	The average fraction of object pixels contained within its skeleton
	SLF7.83	The average fraction of object fluorescence contained within its skeleton
	SLF7.84	The average ratio of the number of branch points in skeleton to length of skeleton
SLF8	SLF8.1 to 8.32	32 features selected from SLF7 using stepwise discriminant analysis
SLF12	SLF12.1 to 12.8	SLF8.1 to 8.8, the smallest feature set able to achieve 80% accuracy
SLF13	SLF13.1 to 13.31	31 features selected from SLF7 and SLF2.17-2.22 using stepwise discriminant analysis

# DTE in PC DTX – analysis “Per Image”



# Unimodal thresholding – MT area (Rosin P.L. Pattern recognition)

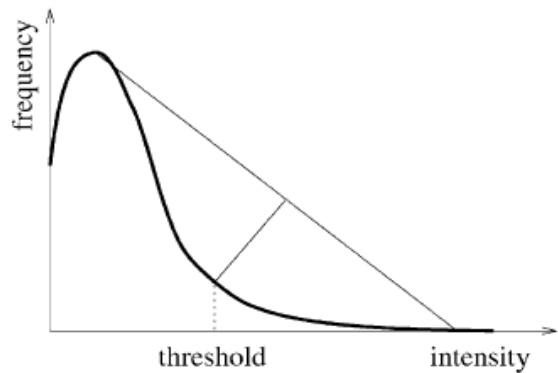
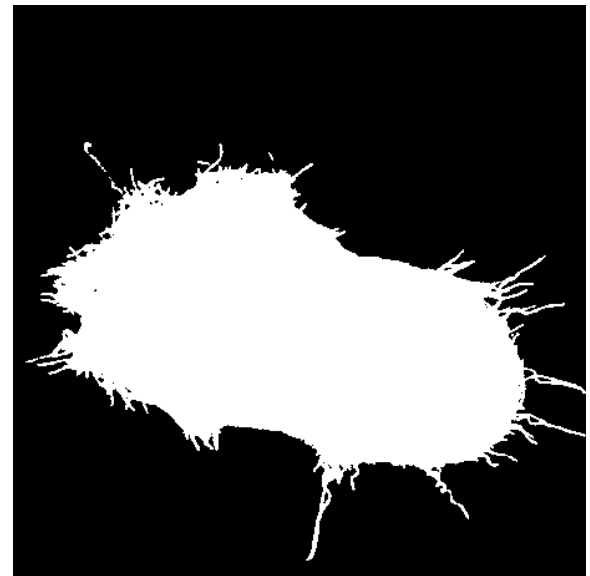


Fig. 1. Procedure for determining threshold from intensity histogram.



# Variance of the MT areas

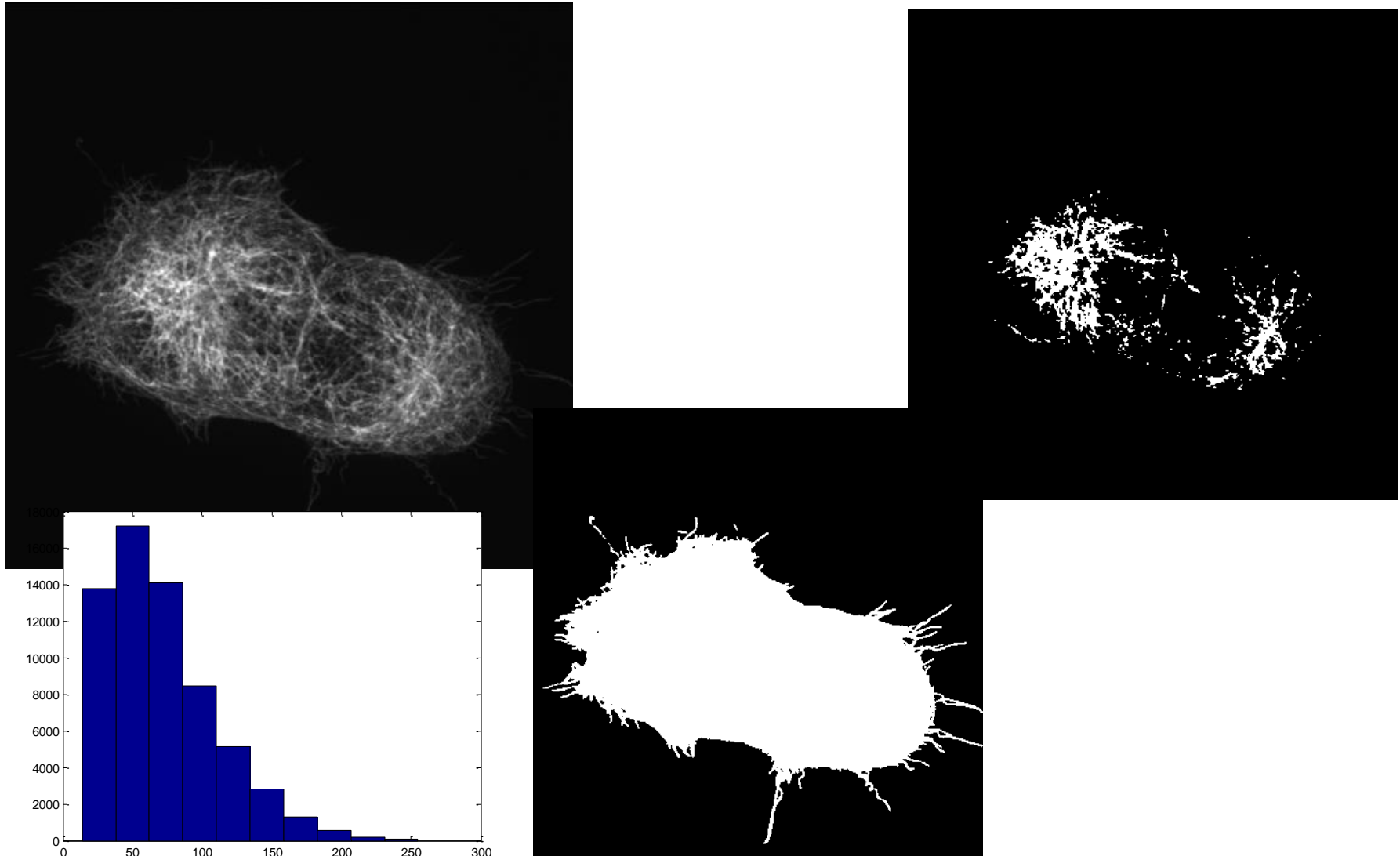
- Variance of pixel intensity measures dispersion, how far are the numbers spread out, i.e. after treatment in the sensitive cells dark pixels vs very bright pixels will increase it

$$\text{variance} = \sigma^2 = \frac{\sum (x_r - \mu)^2}{n}$$

$$\text{standard deviation } \sigma = \sqrt{\frac{\sum (x_r - \mu)^2}{n}}$$

$\mu$  = mean

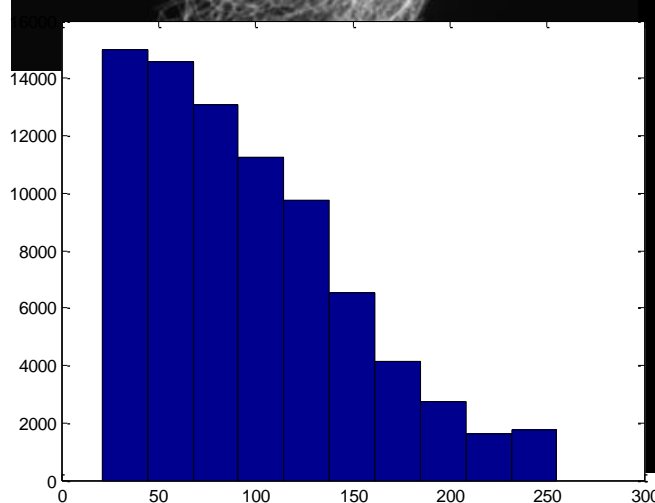
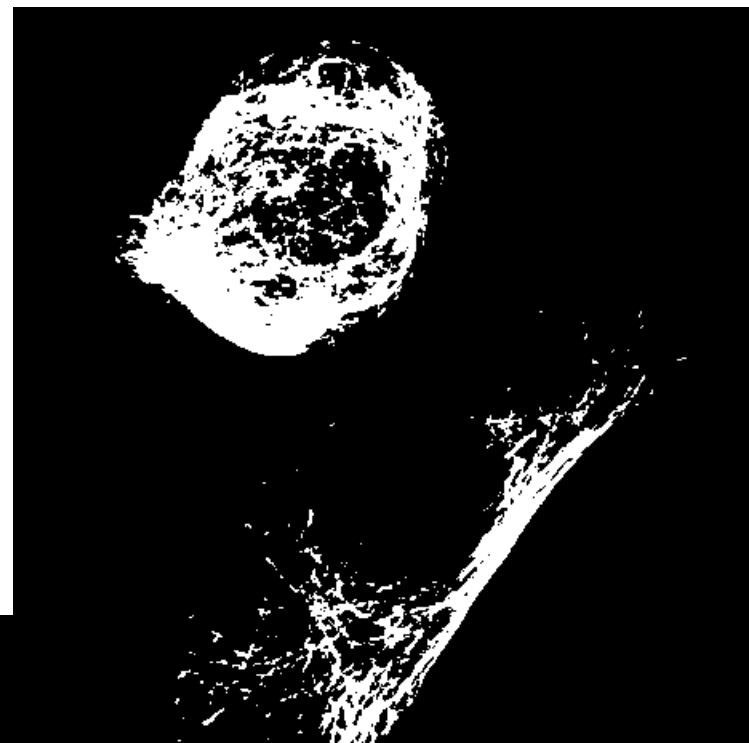
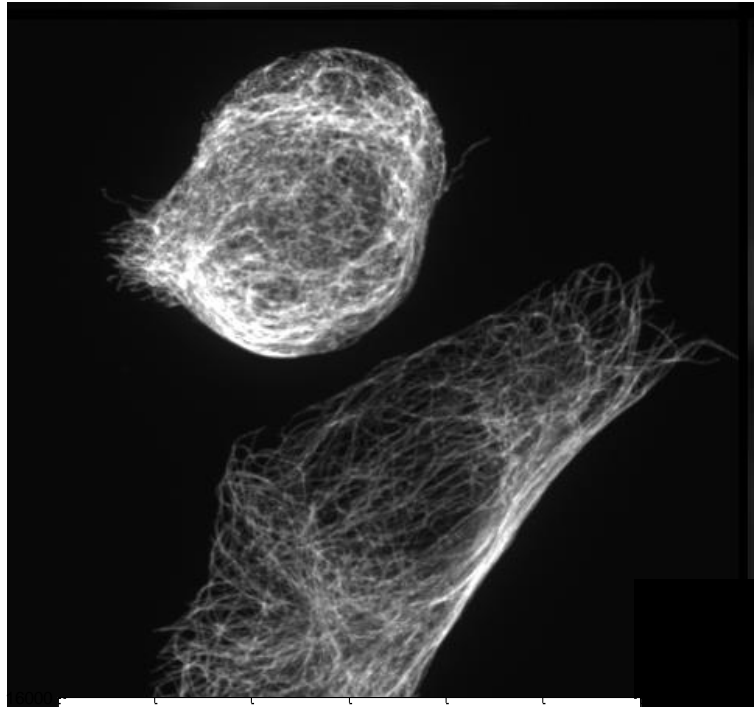
ERG-, **untreated**  
11% cellular area consists of bright MTs  
Max I = 255, med = 64



ERG-, DTX 10 nM

29% cellular area consist of bright MTs

Max I = 255, med = 87



# High level of variability

- ERG- -> more images

Std 39, 54, 41, 61

Var 1543, 2915, 1700, 3778